Terrain physical properties derived from orbital data and the first 360 sols of Mars Science Laboratory Curiosity rover observations in Gale Crater

R E Arvidson, P. Bellutta, F. Calef, A A Fraeman, J B Garvin, Olivier Gasnault, J A Grant, J P Grotzinger, V E Hamilton, M. Heverly, et al.

AGU PUBLICATIONS

JGR

Journal of Geophysical Research: Planets

RESEARCH ARTICLE
10.1002/2013JE004605

Special Section:
Results from the first 360 Sols of the Mars Science Laboratory Mission: Bradbury Landing through Yellowknife Bay

Key Points:
- Curiosity landing site consolidated bedrock covered by packed sand with clasts
- Curiosity drill site is alluvial-lacustrine bedrock unit with little soil cover
- Rover slip/skid dominated by terrain tilt and wheel-surface material shear modulus

Correspondence to:
R. E. Arvidson,
arvidson@wunder.wustl.edu

Citation:
Arvidson, R. E., et al. (2014), Terrain physical properties derived from orbital data and the first 360 sols of Mars Science Laboratory Curiosity rover observations in Gale Crater, *J. Geophys. Res. Planets*, *119*, 1322–1344, doi:10.1002/2013JE004605.

Received 31 DEC 2013
Accepted 18 MAY 2014
Accepted article online 22 MAY 2014
Published online 17 JUN 2014

Terrain physical properties derived from orbital data and the first 360 sols of Mars Science Laboratory Curiosity rover observations in Gale Crater

R. E. Arvidson[1], P. Bellutta[2], F. Calef[2], A. A. Fraeman[1], J. B. Garvin[3], O. Gasnault[4], J. A. Grant[5], J. P. Grotzinger[6], V. E. Hamilton[7], M. Heverly[2], K. A. Iagnemma[8], J. R. Johnson[9], N. Lanza[10], S. Le Mouélic[11], N. Mangold[11], D. W. Ming[12], M. Mehta[13], R. V. Morris[12], H. E. Newsom[14], N. Rennó[15], D. Rubin[16], J. Schieber[17], R. Sletten[18], N. T. Stein[1], F. Thuillier[11], A. R. Vasavada[2], J. Vizcaino[13], and R. C. Wiens[10]

[1]Department of Earth and Planetary Sciences, Washington University, St. Louis, Missouri, USA, [2]Jet Propulsion Laboratory, California Institute of Technology, Pasadena, California, USA, [3]Sciences and Exploration Directorate, NASA Goddard Space Flight Center, Greenbelt, Maryland, USA, [4]IRAP, Université de Toulouse (UPS-OMP)/CNRS, Toulouse, France, [5]Center for Earth and Planetary Studies, National Air and Space Museum, Smithsonian Institution, Washington, District of Columbia, USA, [6]Division of Geologic and Planetary Sciences, California Institute of Technology, Pasadena, California, USA, [7]Southwest Research Institute, Boulder, Colorado, USA, [8]Department of Mechanical Engineering, Massachusetts Institute of Technology, Cambridge, Massachusetts, USA, [9]Johns Hopkins Applied Physics Laboratory, Laurel, Maryland, USA, [10]Los Alamos National Laboratory, Los Alamos, New Mexico, USA, [11]Laboratoire Planétologie et Géodynamique de Nantes, LPGN/CNRS UMR6112 and Université de Nantes, Nantes, France, [12]NASA Johnson Space Center, Houston, Texas, USA, [13]NASA Marshall Space Flight Center, Huntsville, Alabama, USA, [14]Institute of Meteoritics, University of New Mexico, Albuquerque, New Mexico, USA, [15]Ocean, Atmospheric, and Space Sciences, University of Michigan, Ann Arbor, Michigan, USA, [16]Department of Earth and Planetary Sciences, University of California, Santa Cruz, California, USA, [17]Department of Geological Sciences, Indiana University, Bloomington, Indiana, USA, [18]Department of Earth and Space Sciences, University of Washington, Seattle, Washington, USA

Abstract Physical properties of terrains encountered by the Curiosity rover during the first 360 sols of operations have been inferred from analysis of the scour zones produced by Sky Crane Landing System engine plumes, wheel touch down dynamics, pits produced by Chemical Camera (ChemCam) laser shots, rover wheel traverses over rocks, the extent of sinkage into soils, and the magnitude and sign of rover-based slippage during drives. Results have been integrated with morphologic, mineralogic, and thermophysical properties derived from orbital data, and Curiosity-based measurements, to understand the nature and origin of physical properties of traversed terrains. The hummocky plains (HP) landing site and traverse locations consist of moderately to well-consolidated bedrock of alluvial origin variably covered by slightly cohesive, hard-packed basaltic sand and dust, with both embedded and surface-strewn rock clasts. Rock clasts have been added through local bedrock weathering and impact ejecta emplacement and form a pavement-like surface in which only small clasts (<5 to 10 cm wide) have been pressed into the soil during wheel passages. The bedded fractured (BF) unit, site of Curiosity's first drilling activity, exposes several alluvial-lacustrine bedrock units with little to no soil cover and varying degrees of lithification. Small wheel sinkage values (<1 cm) for both HP and BF surfaces demonstrate that compaction resistance countering driven-wheel thrust has been minimal and that rover slippage while traversing across horizontal surfaces or going uphill, and skid going downhill, have been dominated by terrain tilts and wheel-surface material shear modulus values.

1. Introduction

The Mars Science Laboratory Curiosity rover touched down on the hummocky plains (HP) at the Bradbury Landing Site within Gale Crater on 5 August 2012 (Pacific Daylight Time) [*Grotzinger et al.*, 2014] (Figures 1 and 2). By sol 52 Curiosity traversed eastward for 451 m across HP surfaces and arrived at the entrance to Yellowknife Bay (YKB), a valley where a topographically lower bedded fractured unit (BF) is exposed (Table 1). On sol 125 the rover descended into YKB and afterward acquired its first drill samples in outcrops of the BF Sheepbed mudstone [*Grotzinger et al.*, 2014]. After completion of remote sensing and in situ measurements, Curiosity began a series of traverses across HP surfaces to cover the 8.6 km distance needed to get to the base of Mount

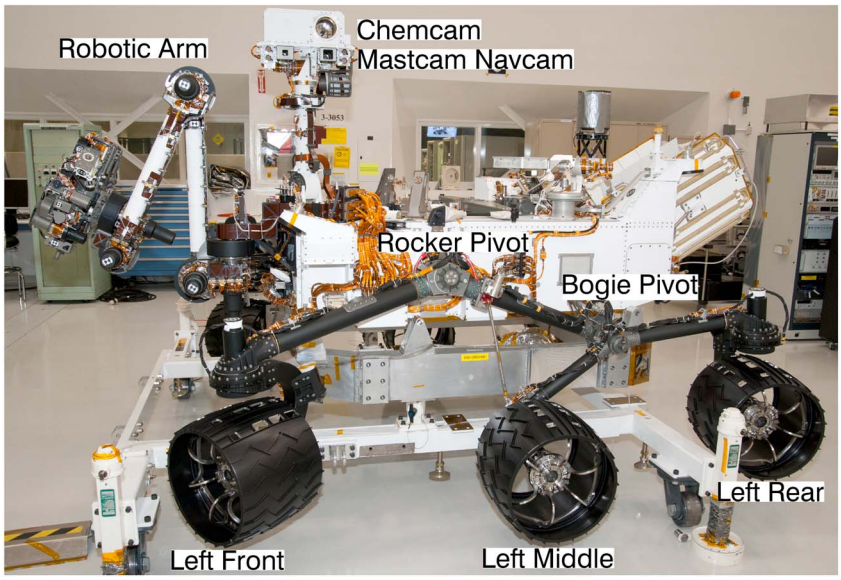

Figure 1. View of Curiosity at the Jet Propulsion Laboratory with focus on wheels and suspension system on the left side of the rover. The rocker pivot is where the suspension system, and wheels are attached to the rover body. The bogie portion of the system is free to pivot about the bogie pivot point, whereas the rocker pivot rotates the opposite way relative to the same pivot on the right side suspension system. For scale the wheels are 0.50 m in diameter.

Sharp (Figures 3 and 4). By sol 360 Curiosity had covered a total traverse distance of 1828 m from the Bradbury Landing Site (Table 1) [*Vasavada et al.*, 2014].

The intent of this paper is to summarize surface and shallow subsurface physical properties for the HP and BF surfaces traversed by Curiosity during the first 360 sols (Figures 3 and 4), combining analyses of orbital data with measurements from Curiosity, including effects of surface scour by the Sky Crane Landing System (SCLS) [*Steltzner et al.*, 2010] engine plumes, wheel touch down dynamics and resultant surface modification, the extent to which rocks were imprinted into soil or broken during wheel passages, variations in the sizes of pits in rocks and soils produced by the ChemCam laser, and modeling of rover traverses to retrieve terramechanics properties. The latter approach employs engineering telemetry and other data obtained during traverses to use the rover as a "virtual instrument" to retrieve soil pressure-sinkage and terrain shear modulus properties [e.g., *Zhou et al.*, 2014]. Results from scooping and other activities at Rocknest, a cluster of rocks that trapped wind-blown sand, and the mechanics of drilling in YKB (Figure 4), will be covered in future publications. Key results from the scooping and drilling campaigns are integrated into the synthesis of physical properties presented at the end of this paper. Because physical properties retrieved depend on how and where the rover was driven (e.g., driving over large rocks was

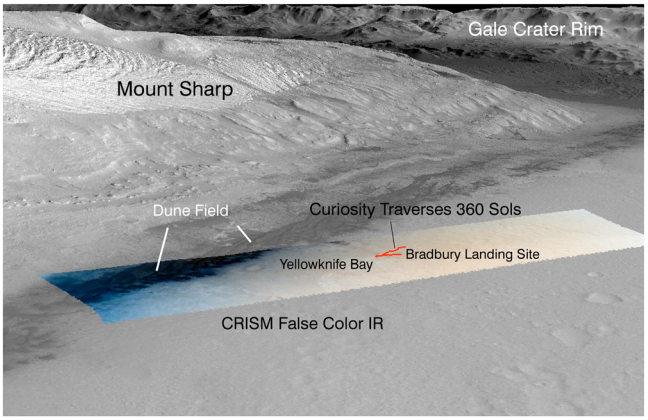

Figure 2. HiRISE-based mosaic and associated digital elevation map were used to generate perspective view of plains on the floor of Gale Crater, together with the northern portion of Mount Sharp. View is from the northeast looking toward the southwest. CRISM FRS00028346 false color IR composite is overlain, and the landing site and traverses through sol 360 are shown. The entrance to Yellowknife Bay is where Curiosity conducted its first drilling and associated CheMin and SAM measurements before starting on traverses to Mount Sharp. For the CRISM image the following bands were used to generate the composite: blue = 1.0800 μm, green = 1.5066 μm, and red = 2.5295 μm.

Table 1. Drive Sol Summary for First 360 Sols

Earth Date	Sol	Drive Distance (m)	Activity
21 Aug 12	16	7.0	Mobility checkout with full wheel turns and IMU measurements
26 Aug 12	21	4.9	Place Dynamic Albedo of Neutrons (DAN) over Goulburn Scour, allow ChemCam to reach new targets
27 Aug 12	22	15.1	Drive to Glenelg and position for long-baseline Mastcam observation
29 Aug 12	24	21.5	Drive to Glenelg with guarded arc checkout
31 Aug 12	26	29.8	Drive to Glenelg with visual odometry checkout
3 Sep 12	29	30.6	Drive to Glenelg
13 Sep 12	38	32.3	Drive to Glenelg, look for APXS/ChemCam cross calibration target, begin VO-based slip checks
14 Sep 12	39	21.7	Drive to Glenelg, look for APXS/ChemCam cross-calibration target
15 Sep 12	40	37.2	Drive to Glenelg, look for APXS/ChemCam cross-calibration target
16 Sep 12	41	27.0	Drive to Glenelg, look for APXS/ChemCam cross-calibration target, first active DAN during traverse
17 Sep 12	42	32.0	Drive to Jake_Mateijevic cross-calibration rock target
18 Sep 12	43	30.0	Drive to Jake_Mateijevic cross-calibration rock target
20 Sep 12	45	4.5	Precision approach using VO to Jake_Mateijevic cross-calibration target
23 Sep 12	48	41.7	Drive to Glenelg after first "stow and go"
24 Sep 12	49	30.7	Drive to Glenelg
25 Sep 12	50	48.9	Drive to Glenelg, look for sand target for first scoop sample
27 Sep 12	52	36.3	Drive to Glenelg, look for sand target for first scoop sample
28 Sep 12	53	2.1	Precision approach to Bathurst Inlet rock target
30 Sep 12	55	23.5	Drive to Rocknest sand scoop target
1 Oct 12	56	5.9	Precision approach to scuff location in Rocknest sand scoop target
2 Oct 12	57	1.8	Scuff Rocknest sand scoop target
4 Oct 12	59	5.5	Position rover for sand scooping activity at Rocknest
15 Nov 12	100	1.9	Precision approach to Rocknest3 sand target for arm activities
17 Nov 12	102	25.3	Drive to Point Lake after Rocknest3 APXS measurements
27 Nov 12	111	1.9	Drives to position Bell_Island rock target for in situ measurements
6 Dec 12	120	34.6	Drive to Shaler outcrop
7 Dec 12	121	24.2	Drive to Yellowknife Bay
8 Dec 12	122	1.0	Drive to Yellowknife Bay
9 Dec 12	123	19.4	Drive to Yellowknife Bay
10 Dec 12	124	14.0	Drive to Yellowknife Bay
11 Dec 12	125	26.1	Drive into Yellowknife Bay
13 Dec 12	127	32.8	Drive to contact in Yellowknife Bay
16 Dec 12	130	5.6	Explore Yellowknife Bay
19 Dec 13	133	21.7	Drive to Grandma's_House imaging location in Yellowknife Bay
3 Jan 13	147	3.0	Bump to Snake River in Yellowknife Bay
7 Jan 13	151	0.7	Bump to units 1–2 contact in Yellowknife Bay
8 Jan 13	152	2.4	Finish bump to units 1–2 contact in Yellowknife Bay
15 Jan 13	159	1.4	Bump to new arm target in Yellowknife Bay
18 Jan 13	162	9.0	Bump to John_Klein in Yellowknife Bay
19 Jan 13	163	1.9	Crush vein by rolling over it
20 Jan 13	164	3.2	Finish vein crushing
22 Jan 13	166	3.3	Touch and go and bump to John_Klein drill location
11 May 13	272	3.1	Bump to Cumberland drill location
13 May 13	274	0.7	Finish bump to Cumberland drill location
4 Jun 13	295	6.3	Begin active DAN campaign across Yellowknife Bay
6 Jun 13	297	19.8	Continue active DAN campaign across Yellowknife Bay
8 Jun 13	299	8.4	Continue active DAN campaign across Yellowknife Bay
10 Jun 13	301	12.0	Finish DAN active campaign and drive to Point Lake
11 Jun 13	302	2.7	Arrive at Point Lake
16 Jun 13	307	31.8	Drive to Shaler
17 Jun 13	308	22.0	Continue drive to Shaler
18 Jun 13	309	1.8	Continue drive to Shaler
22 Jun 13	313	9.3	Continue drive to Shaler
26 Jun 13	317	6.8	Continue drive to Shaler
3 Jul 13	324	18.0	Exit Glenelg to Rapid Transit Route (RTR) to Mount Sharp
6 Jul 13	327	40.0	Continue to exit Glenelg to RTR
9 Jul 13	329	41.1	Continue to exit Glenelg to RTR
11 Jul 13	331	28.0	Start RTR to Mount Sharp

Table 1. (continued)

Earth Date	Sol	Drive Distance (m)	Activity
13 Jul 13	333	15.5	RTR to Mount Sharp
15 Jul 13	335	38.2	RTR to Mount Sharp
16 Jul 13	336	32.9	RTR to Mount Sharp
17 Jul 13	337	37.7	RTR to Mount Sharp
18 Jul 13	338	34.1	RTR to Mount Sharp
20 Jul 13	340	100.3	RTR to Mount Sharp
22 Jul 13	342	62.4	RTR to Mount Sharp
23 Jul 13	343	33.7	RTR to Mount Sharp
24 Jul 13	344	70.1	RTR to Mount Sharp
25 Jul 13	345	70.2	RTR to Mount Sharp
27 Jul 13	347	60.1	RTR to Mount Sharp
29 Jul 13	349	70.2	RTR to Mount Sharp
31 Jul 13	351	85.1	RTR to Mount Sharp
3 Aug 13	354	57.1	RTR to Mount Sharp
5 Aug 13	356	50.0	RTR to Mount Sharp
7 Aug 13	358	35.0	RTR to Mount Sharp

prohibited), a synopsis of the drive modes and paths is summarized in the next section of this paper. Finally, the term soil is used throughout the paper and is meant to connote loose material on planetary surfaces produced by a variety of processes, including, but not limited to materials that have been altered in situ with definable vertical textural or compositional profiles.

2. First 360 Sols: Mission and Mobility Overviews

The primary scientific target for the Mars Science Laboratory Mission was chosen to be Mount Sharp, a ~85 km by 5 km high mound exposing layered sedimentary rock and located within the 154 km diameter Gale Crater [*Grotzinger et al.*, 2012]. The SCLS required that the landing site be located in relatively flat, rock-free terrain and thus Curiosity touched down onto an HP surface (Bradbury Landing Site) located to the north of Mount Sharp (Figures 2 and 3). Initial observations by Curiosity after landing, combined with the regional morphologic and geologic contexts provided by orbital observations, showed that the HP surface is dominated by hard-packed soil and rock clasts that overlie conglomeratic bedrock [*Williams et al.*, 2013]. The bedrock was inferred to have been deposited at the distal end of a coalescing alluvial fan system extending from the northern wall and rim of Gale Crater [*Williams et al.*, 2013].

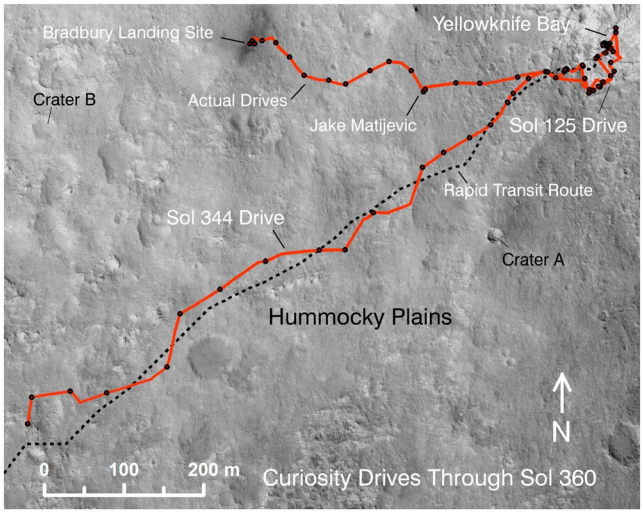

Figure 3. Portion of a HiRISE image overlain with Curiosity traverses for the first 360 sols, the Bradbury Landing Site, and dark zone produced by interaction of the Sky Crane Landing System (SCLS) thruster plumes with the surface. The Rapid Transit Route (RTR) was generated by automatically, finding the most efficient route that avoided key hazards identified from orbital data, such as large rocks. Actual routes were derived from end of drive imaging and were designed to stay close to the RTR while staying on topographic meshes and avoiding obstacles not recognized in developing the RTR. Crater A looks relatively fresh, whereas crater B does not. A range of crater preservation states is evident in the image and is evidence for considerable reworking of terrains traversed by Curiosity. HiRISE frame ESP_028335_1755_red.jp2 acquired on 11 August 2013.

Detailed mapping before landing using orbital data indicated that bedrock exposures in YKB might enable sampling of a BF lacustrine facies (distal end of the alluvial fan complex) that stratigraphically underlies HP or represents late-stage deposits in a preexisting valley

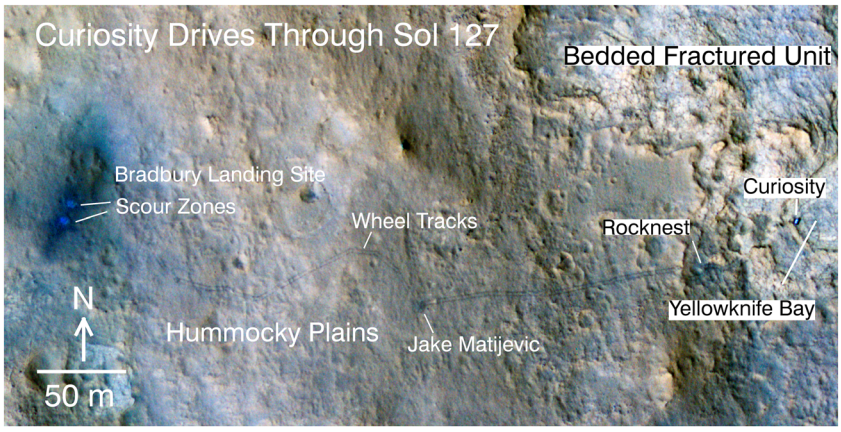

Figure 4. False color HiRISE image emphasizing the scour zones associated with SCLS thruster plumes impacting the surface, producing the two bright scoured areas on either side of the rover touch down spot and the more extended dark blue area surrounding these areas. Also evident are the dark tracks generated by Curiosity's wheels during drives to Yellowknife Bay. Jake Matijevic was a rock that the rover was diverted to for initial in situ measurements. Rocknest is a cluster of boulder on the edge of Yellowknife Bay that trapped wind-blown sand and is the location for Curiosity's first scooping of loose material for delivery to SAM and CheMin. Curiosity can be seen within the Bedded Fractured unit. Portion of HiRISE frame ESP_030313_1755 and displayed with blue color using the blue-green bands (0.4–0.6 μm), green using the red band (0.55–0.85 μm), and red using the IR band (0.8–1.0 μm).

[*Grotzinger et al*., 2014]. Given that a lacustrine environment might have provided conditions necessary for habitability, the decision was made to first drive to YKB to characterize and sample these materials. After initial mobility check-out procedures, a series of traverses was undertaken, with stops at the rock Jake_Matijevic to conduct compositional and textural measurements using Mast and Arm-based instruments [*Stolper et al*., 2013] (Figures 3 and 4). A stop was also made in the Rocknest cluster of boulders with trapped wind-blown sand (Figure 4) to conduct the first scooping and delivery of samples to Chemistry and Mineralogy analyzer instrument (CheMin) and Sample Anaylsis at Mars (SAM) for detailed mineralogic and volatile analyses, respectively [*Blake et al*., 2013; *Leshin et al*., 2013]. Curiosity then traversed into YKB and drilled into the Sheepbed mudstone unit. The drill samples from the John Klein and Cumberland targets were found to contain trioctahedral smectite, likely produced by in situ aqueous alteration [*Vaniman et al*., 2014], and overall, the data collected were found to be consistent with an ancient lacustrine environment. After examining other units within YKB, Curiosity began its long set of traverses along the HP surfaces to cover the ~8.6 km to the base of Mount Sharp.

Traverses through the 360 sol period covered in this paper were accomplished in a "blind mode" in which the rover was commanded to drive along a set of Ackerman Arcs to given waypoints defined in digital elevation maps (DEMs) generated from end-of-drive navigational camera (Navcam) stereo imaging data, augmented by use of High Resolution Imaging Science Experiment (HiRISE) images and associated DEM products. Ackerman Arcs are implemented by commanding wheel drive actuator angular velocities to move the rover along an arc with a specified radius of curvature. This allows curved trajectories with minimum wheel sideways slip. Threshold settings on rover tilt (based on accelerometer measurements) and wheel actuator currents were implemented to stop the vehicle if the tilt became too high or the motor currents exceeded some critical value, e.g., due to extensive wheel sinkage into soil and consequent high compaction resistance. On sol 38 the rover began automatically assessing the magnitude of slippage during drives using visual odometry (VO) in which stereo imaging of fixed locations was accomplished periodically during drives and actual distances covered were compared to commanded distances (see *Maimone et al*. [2007] for VO description). Typically, between 0.5 to 1.0 m spacing was used between stereo acquisition stations for a slippage determination. Slippage, S, is defined as

$$S = 1 - d_a/d_c \quad (1)$$

where d_a is the actual distance traversed between the VO stereo data acquisitions and d_c is the commanded distance. Although not computed on board, ground-based processing of VO data allowed both the sign and

magnitude of slip to be calculated. Positive slippage occurs when the rover travels less than commanded, whereas negative slippage (skid) occurs when the rover travels further than requested. Rover slippage is in part both associated with wheels sinking into deformable soil, increasing compaction resistance and leading to increased slippage. Slippage is also strongly influenced by local slopes, i.e., when driving upslope, the increased fraction of the rover weight acting in the opposite direction from travel leads to increased slippage. Skid is associated with downhill portions of drives where the downhill component of gravity leads to a situation in which the rover travels further than commanded. When driving on horizontal surfaces with minimum compaction resistance slippage is controlled by the soil shear modulus [e.g., *Wong*, 2001].

During the extended stay in YKB to acquire and analyze drill samples and survey the various strata, plans were developed to generate a "rapid transit route" (RTR) to the base of Mount Sharp. Digital hazard maps were generated that the rover would need to avoid along candidate routes, including bedrock-dominated slopes steeper than 25°, sandy slopes steeper than 12.5°, aeolian dunes and ripples, and rocks taller than one-wheel diameter (0.50 m). Relatively bright, bland areas were also avoided since these might be dominated by soft aeolian soils that could lead to significant wheel sinkage, increased compaction resistance, high slippage, and possible embedding (i.e., ~100% slip). These maps were generated using HiRISE color images and elevation maps generated from HiRISE data [*McEwen et al.*, 2007]. Sandy and rocky areas were inferred from visual analysis of the images and rock size distributions were mapped using an automated algorithm developed by *Huertas et al.* [2006]. The combination of these hazard "layers" was used with the Field D* automated path planner [*Ferguson and Stentz*, 2005] to generate the RTR. Field D* chose shortest routes to the base of Mount Sharp that avoided obstacles using 10 m wide cells for its calculations. The RTR has been followed, with tactical mark-ups by rover planners working with the advice of science team members assigned to provide advice about terrain properties that might affect drives. Actual paths have deviated about the RTR to avoid obstacles such as rock fields and sand-filled craters not evident in the hazard layers mapped from orbital data (Figure 3). Paths also deviated from the RTR based on how far a given DEM (so-called mesh) derived from Navcam stereo images extended in the drive direction. Longer drives on laterally extensive DEM meshes were favored over shorter drives that moved the rover along the exact RTR, given lack of hazards along the long-drive direction.

3. Terrain Properties Based on Orbital Data

HiRISE images and associated DEMs [*McEwen et al.*, 2007], Compact Reconnaissance Imaging Spectrometer for Mars (CRISM)-based spectral reflectance values [*Murchie et al.*, 2007], and Thermal Emission Imaging System (THEMIS)-based estimates of thermal inertia (TI) [*Christensen et al.*, 2004; *Fergason et al.*, 2012] provide important information on terrain properties for areas traversed by Curiosity. This section of the paper focuses on use of these orbital data sets to place regional constraints on HP and BF surface and shallow subsurface properties, which are then combined with rover-based observations to understand the terrains encountered by Curiosity.

False color HiRISE data were acquired when Curiosity was in YKB (Figure 4). Of particular interest is the ~50 m wide dark bluish zone with two bright blue areas centered on Curiosity's touch down location and interpreted to be due to scour by the SCLS thruster plumes. The SCLS included eight thrusters arranged in four pairs and fueled by monopropellant hydrazine. The thrusters became active at an altitude of ~1.8 km. At ~20 m altitude four of the thrusters were turned off, and Curiosity was lowered from the bottom of the SCLS to the surface wheels first on three 7.6 m tethers and an electrical cable. After touch down, these were cut, and the SCLS flew away from the touch down site. The scour patterns produced by the thruster plumes provide important information on surface and shallow subsurface physical properties, excavating and transporting soil away from the landing site and exposing underlying conglomeratic bedrock immediately below the final descent path [e.g., *Schieber et al.*, 2013; *Williams et al.*, 2013]. The thruster plume interactions with the HP surface are quantitatively modeled in a subsequent portion of this paper. For this section the spectral and thermal properties associated with the areas disturbed by the thruster plumes are summarized, together with surrounding undisturbed areas.

The color and albedo patterns evident in the false color HiRISE image can be placed in a more quantitative context using spectral reflectance data from CRISM and THEMIS-based TI values for HP natural and disturbed, BF, and dune surfaces. A CRISM full-resolution targeted mode short (FRS) observation was acquired over

Table 2. CRISM Observation Details[a]

Parameter	Details
Acquisition date	13 January 2013
Center latitude	4.581°S (areocentric)
Center longitude	137.452°E (areocentric)
Martian season	Ls = 244°, late southern spring
Retrieved dust aerosol opacity	0.95 at a 0.9 μm reference wavelength from Mastcam
Retrieved CO_2 pressure for central portion of scene	8.7 mbar from REMS
Retrieved surface photometric function	Henyey-Greenstein two-term single-particle phase function asymmetry factor = 0.26, forward fraction = 0.30
Hapke parameters	

[a]CRISM FRS00028346 observation and processing details. See *Arvidson et al.* [2014] for detailed discussion of processing to retrieve SSA values.

these areas when Curiosity was in YKB. The data have 18 m/pixel spatial resolution and cover 0.362–3.920 μm with a spacing of 6.55 nm/channel [*Murchie et al.*, 2007] (Table 2). CRISM data were first converted to spectral single scattering albedos (SSA), which are the ratio of scattering to scattering and absorption efficiencies and are independent of lighting and viewing conditions. For particulate materials it is controlled by the complex refractive indices and grain sizes of constituent materials. SSA spectra were retrieved by simultaneously modeling atmospheric gases, aerosols, surface scattering, and thermal emission, using the Hapke bidirectional scattering function and discrete ordinates radiative transfer (DISORT)-based radiative transfer code [*Stamnes et al.*, 1988] (see *Arvidson et al.* [2014] for description of the methodology). Thermal contributions were modeled on a pixel-by-pixel basis using Lambert Albedo data derived from the CRISM scene (Lambert Albedo values retrieved from DISORT modeling, using a weighted average over solar wavelengths, corrected for atmospheric gases and aerosols), TI values, and a thermal model [*Hamilton et al.*, 2014] to retrieve surface kinetic temperature for the sol and local solar time of the CRISM observation. The model was calibrated using Curiosity's Remote Environmental Monitoring Station (REMS) surface temperature observations (268 K) [*Sebastián et al.*, 2010] acquired at the same time as the CRISM observation. Retrieved surface kinetic temperatures (~260 to 275 K) were then used to model observed spectral radiances for combined surface and atmospheric scattering and absorption of sunlight and thermal emission, scattering, and absorption.

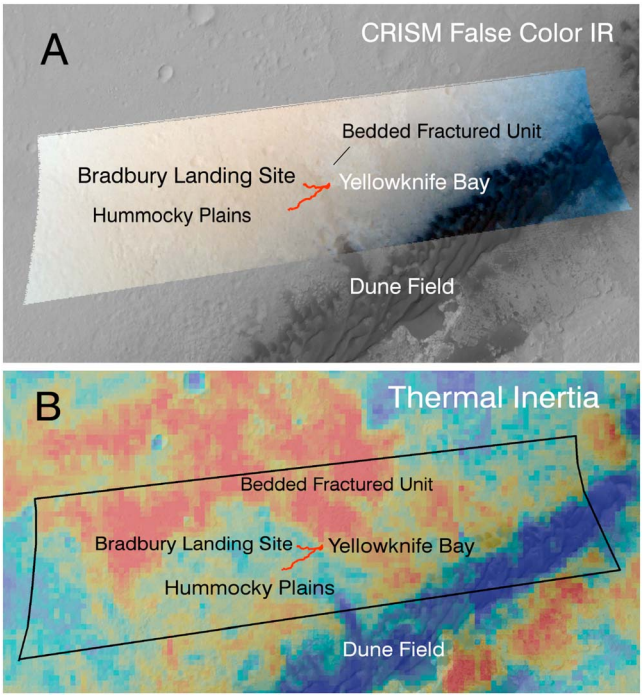

Figure 5. (a) CRISM FRS00028346 false color composite overlain with Curiosity's drives for first 360 sols. Bands are 0.7099, 0.5926, and 0.5340 μm as red, green, and blue. This CRISM scene covers ~ 10 km in its long dimension. (b) THEMIS-based thermal inertia image for region covered by CRISM data and showing drives for first 360 sols. Data from *Fergason et al.* [2012]. Blue colors correspond to low and red to high thermal inertia values, with a dynamic range of ~250 to 550 J m^{-2} K^{-1} $s^{0.5}$.

SSA values at 0.77 μm (wavelength with high S/N for CRISM) and TI-coregistered data (Figure 5) were used to generate a scatterplot for a broad area that includes traverse locations for the first 360 sols of operations (Figures 6a and 6b). The plot is also overlain with global trends for Mars, using SSA values for classical bright (Arabia Terra) and dark (Syrtis Planitia)

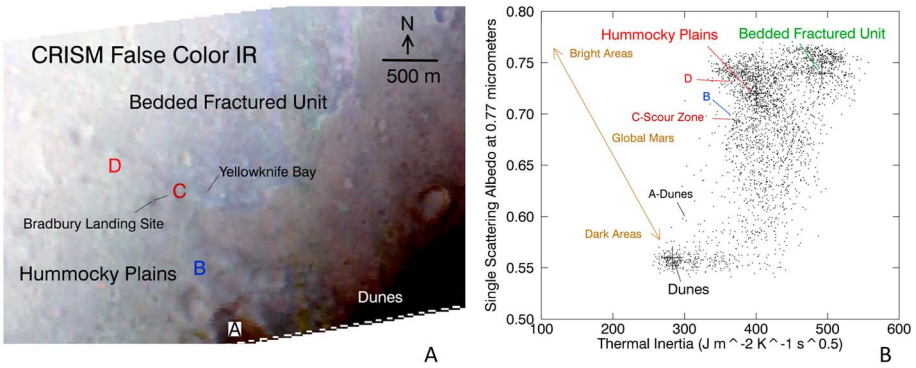

Figure 6. (a) Portion of CRISM false color image (also shown in Figure 5a) contrast enhanced to show local color variations. The surface becomes increasingly bright from the dunes toward the northwest. Data for locations A–D are discussed in the text and shown in Figures 6b and 7. (b) Scatterplot of single scattering albedo (SSA) derived from CRISM data versus thermal inertia from THEMIS, with key locations shown. Data retrieved for CRISM scene and same areas for THEMIS data. Global averages for dark and bright areas are also shown based on data provided in *Putzig et al*. [2005]. Note how data for areas covered by the CRISM scene show increasing thermal inertia with increasing SSA values, opposite to the main trend on Mars. Averages for the hummocky plains and bedded fractured units are shown, along with dunes to the south, and an average of 9 pixels (18 m/pixel) for the dark scour zone centered on the landing site.

areas as derived by *Fox et al*. [2013] from CRISM observations (Figure 6b). The Gusev plains, traversed by Spirit and covered variably by dust, poorly sorted basaltic sands, and rock clasts [*Arvidson et al*., 2004, 2006; *Sullivan et al*., 2011], show a similar trend as global Mars [*Lichtenberg et al*., 2007]. Both the global and Gusev plains have bright areas with low thermal inertias as compared to dark areas, consistent with the presence of bright dust deposits that are thicker than the diurnal thermal skin depth (~1 to 3 cm) [see *Lichtenberg et al*., 2007; *Hamilton et al*., 2014]. For Gale crater the HP, BF, and dune surfaces show an opposite trend in that the bright terrains (HP and BF) have higher thermal inertias as compared to the dark terrain (dunes). Furthermore, HP and BF have higher thermal inertias as compared to the Gusev plains (<400 TI units) [see *Lichtenberg et al*., 2007]. Also shown in the plot is the SSA and TI position of the scour zone (labeled as C, Figure 6a shows location) produced by the thruster plumes, assuming that the TI value (TI data predate the landing) was not changed as a consequence of the plume-induced erosion of soils. The plotted TI value is thus a lower bound since soil was eroded, exposing underlying bedrock. The lowest LA and TI pair is for the dune field to the south of the landing site (A), followed by a relatively dark area between the landing site and the dune field (B). The scour zone (C) has values equivalent to area B and lower than found on the BF surface to the north of the landing site (D).

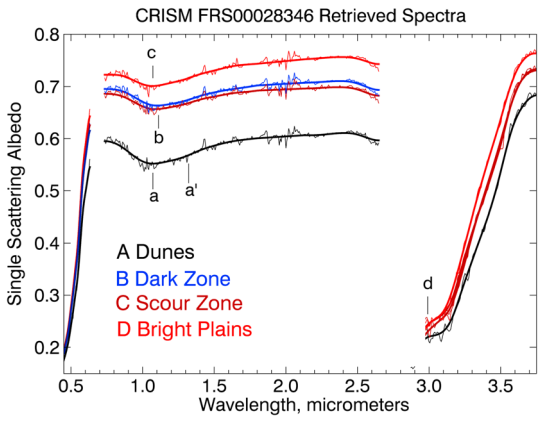

Figure 7. CRISM single scattering albedo spectra for dunes, dark zone north of dunes, scour zone, and undisturbed bright area to NW (i.e., away from the dunes) of the scour zone. Lower case letters delineate absorptions described in the text. The dark zone spectrum longward of 3 μm is hidden under the socur zone spectrum.

CRISM SSA values can also be used to understand the mineralogy of areas A–D (Figure 7). Specifically, SSA spectra from 0.45 to 3.75 μm for areas A–D and their locations in the CRISM scene are shown in Figure 7. All four spectra show a sharp dropoff to low values at wavelengths shorter than ~0.7 μm associated with the ubiquitous presence of dust and its spectral dominance by nanophase iron oxides and associated Fe^{+3} electronic transition features [e.g., *Morris et al*., 2001]. Note that this is even the case for the scour zone, implying that not all dust had been removed. The dune spectrum shows an asymmetrical Fe^{+2} electronic transition feature centered at 1.03 to 1.05 μm (labeled as "a" in Figure 7) with a broad feature centered at ~1.3 μm

(labeled as a′) and interpreted to be due to the presence of olivine [*Seelos et al*., 2013]. The dark area (B) and landing site spectra (C) are similar in magnitude and shape and consistent with a mix of Fe^{+2} silicates (labeled as b) and dust. The spectrum to the north of the landing site (D) shows a shallow feature at this wavelength (labeled as c), consistent with a mix of electronic transition absorptions associated with Fe^{+2} silicates (olivine and pyroxene) [see *Seelos et al*., 2013] and dust [*Morris et al*., 2001]. The presence of olivine and pyroxene is consistent on a regional-scale with the CheMin X-ray diffraction data for wind-blown basaltic sands trapped in the Rocknest cluster of rocks [*Blake et al*., 2013].

Each of the four spectra shown in Figure 7 also exhibits a deep absorption centered at ~2.8 to 2.9 μm (labeled as d). The broad nature of the absorption and similarity in shape for all four spectra is consistent with the presence of H_2O on and/or within surface materials and is typical of the absorption found ubiquitously on Mars [*Jouglet et al*., 2007; *Milliken et al*., 2007]. It is interpreted to be due to the OH stretch and H-O-H bending mode combination absorption of H_2O [e.g., *Clark*, 1999]. The lack of related absorptions centered at ~1.4 and 1.9 μm is consistent with a minor amount of H_2O that is not high enough to show at the shorter wavelength and typically shallower OH and H-O-H combination bands. ChemCam initial laser shots have produced line emission spectra which include moderately strong hydrogen peaks, with values decreasing as the number of shots increased and surface materials were removed by ablation [*Meslin et al*., 2013]. In addition, the CheMin X-Ray diffraction data for both Rocknest wind-blown basaltic sands and YKB John Klein and Cumberland Mudstone drilled samples show evidence for extensive amorphous mineral phases [*Blake et al*., 2013; *Bish et al*., 2013]. It is reasonable to assume that the broad H_2O feature evident in the CRISM spectra is due to fine-grained hydrated materials that coat or cover rocks, together with amorphous grains in soils that carry adsorbed and absorbed H_2O [e.g., *Meslin et al*., 2013].

Combining spectral and thermal inertia data sets allows development of a model for HP and BF surface and near-surface properties. Specifically, relatively bright dust covers the surface with a thickness that increases with increasing distance from the dune field. The dust cannot be thick relative to the diurnal skin depth of ~1–3 cm inferred from the thermal inertia data (also see *Hamilton et al*. [2014] for analysis of REMS data) but must be thicker than the optical skin depth for CRISM (hundreds of micrometers based on opacities of identified minerals and grain sizes). Underlying the dust layer is basaltic soil, rock clasts, and bedrock, with less dust and more basaltic sand closer to the dune field. The dust and basaltic soil layer have been partly excavated in the scour zone by plume-induced erosion and transport of soil material [*Schieber et al*., 2013]. This interpretation is supported by analysis of ChemCam passive spectra for rocks near the landing site, which are some of the darkest spectra observed during the first 360 sols of the mission [*Johnson et al*., 2014]. The basaltic soil is less abundanton over BF (relatively high thermal inertia) as opposed to HP surfaces. This overall interpretation is also supported by the generation of dark wheel tracks as Curiosity traversed toward Yellowknife Bay (Figure 4). Dark wheel tracks were also ubiquitous for the period when the Spirit Rover crossed the Gusev plains on the way to the Columbia Hills and were due to wheels pressing bright surface dust into the pore spaces of underlying dark basaltic sands [*Arvidson et al*., 2004, 2006; *Sullivan et al*., 2011]. A similar process is inferred to produce the dark Curiosity tracks on HP surfaces, consistent with dust covering basaltic sands.

4. Modeling Scour From Skycrane Engine Plumes

In this section analyses are presented based on the extent to which the plumes from the SCLS thrusters scoured the HP surface. Figure 8 shows a portion of a Navcam image mosaic acquired after Curiosity drove away from the touch down location and covers four scoured areas associated with the four thruster plumes interacting with the surface. Figure 9 shows a portion of a Navcam mosaic acquired before the rover began its drives and shows in more detail the Burnside and Goulburn scours generated on the port side of the rover. The natural surface is a rock-strewn soil, with both embedded and surface rock clasts, as detailed by *Yingst et al*. [2013]. Also shown in Figure 9 are modeled streamline traces from computational fluid dynamics simulations [*Mehta et al*., 2013] of the plumes interacting with the surface and rover. Note that some of the streamlines show trajectories from the surface to the rover deck. Navcam data also show that granule- to sand-sized grains were deposited onto the rover deck as ejecta from the scouring events (Figure 9) [*Schieber et al*., 2013]. A Mast Camera (Mastcam) color image is also included as an inset in Figure 9 that shows that the Goulburn scour event excavated soil and exposed underlying bedrock. Curiosity drove over the Goulburn scour and imaging observations showed that the bedrock is a conglomerate [*Williams et al*., 2013].

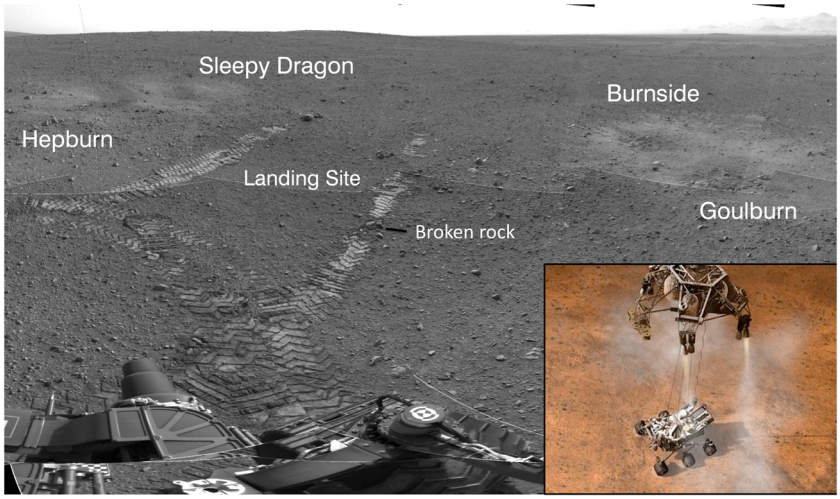

Figure 8. Navcam mosaic acquired on sol 16 looking back at the four scour zones produced by the SCLS engine plumes and the landing site for Curiosity, which landed wheels down. Inset in bottom right is a graphic illustrating touch down. Front of the rover during landing was facing to the lower left of the image. Note the lack of wheel penetration into the soil, and a broken rock that would have been underneath the left middle wheel as it touched down.

Figure 10 shows a digital elevation model generated from Navcam stereo data for the Burnside and Goulburn scour zones. The elevation data show that the maximum scour depth for Goulburn is 6.7 cm, whereas it is 5.9 cm for Burnside. Approximate widths for the scour zones are 1.33 m and 1.74 m, respectively. Estimated eroded volumes are 0.0538 m^3 and 0.109 m^3. The four intense scour zones evident in the HiRISE false color image are merged into the two bright blue zones on either side of the landing location (Figure 4). These bright blue areas correspond to the most intense portions of plume-surface interactions. Clearly, the plumes interacted with surrounding surfaces at higher elevations and were capable of entraining and transporting bright dust and perhaps some soil over the lateral length scales of ~50 to 100 m to produce the dark zone discussed in the previous section of this paper.

A semiempirical engineering model [*Mehta et al.*, 2013] was used to determine plume-induced erosion rates as a function of depth to retrieve soil properties for the four scour zones. The model employs nondimensional

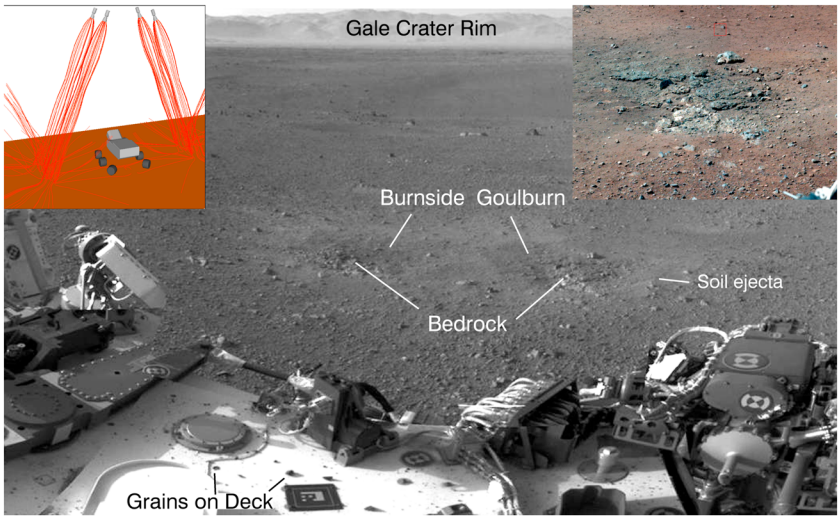

Figure 9. Portion of Navcam mosaic acquired on sol 3 covering two of the scour zones generated by plumes from the SCLS (see graphic in top left). Note grains on rover deck that were emplaced by ejection of grains from the scour zones. Bedrock was exposed by plume-induced erosion as shown by the Mastcam color image inset in the upper right. Mastcam data acquired on sol 13.

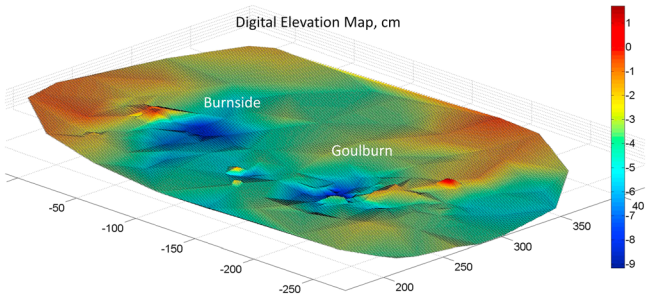

Figure 10. Digital elevation map (DEM) of Burnside and Goulburn scours on the port of left side of the rover during and after landing. DEM generated from Navcam stereo images. Scour extended 5–9 cm beneath the surface before encountering bedrock underlying the soil.

scaling analyses and was validated against extensive ground test data for the Phoenix Lander, along with three SCLS thruster ground tests [*Mehta et al*., 2011]. Table 3 shows engineering model results for the ground tests for varying soil cohesions and particle sizes, along with the ratio of crater volume erosion rate to descent engine mass flow rate, and the normalized cutoff altitude for the descent engines. The engine thrust level and initial ground slope angle shown in Table 3 are approximately the same for each test to provide adequate comparisons. The inferred crater volume to descent mass rates for the scour zones are similar to the Mars Science Laboratory (MSL)-2 and MSL-8 tests, with models run with a particle size ~100 um, with a cohesive strength ~1.3 KPa. This strength is typical of fine-grained, weakly cohesive Martian and terrestrial soils [*Sullivan et al*., 2011]. Based on the test and flight data comparisons, the first dominant erosion mechanism mode for the plumes above the scour zones was shear failure of the slightly cohesive soils, with subsequent soil entrainment until the thruster plumes exposed the underling bedrock. The dominant erosion mechanism then became viscous shear erosion, which removed the remaining soil particles from the exposed bedrock.

5. Landing On and Driving Over Soils and Rocks

Curiosity landed with wheels down onto HP surface with an impact velocity of 0.63 m/s, based on onboard inertial measurement unit (IMU) data. Navcam images looking back at the landing site show only shallow wheel imprints in the soil-dominated surface and one rock that may have been broken during touch down of the left middle wheel, but not pushed into the subsurface (Figure 8). Basic terramechanics equations show for deformable that soil resistance increases with increasing pressure-induced sinkage of wheels as a power law relationship until a force balance is achieved between the wheel load and the resisting soil [e.g., *Wong*, 2001]. To simulate the minimal imprints of the wheels into the HP surface the Artemis software code was used that simulates normal and shear stresses between wheels and soil surfaces [*Zhou et al*., 2014]. Artemis employed a Curiosity mechanical rover model developed for rover drop tests [*White et al*., 2012] and modeled descent and landing for all six wheels and the rover, including propagating stresses back into the rocker-bogie suspension system (Figure 1). Deceleration and maximum normal stresses were modeled between wheel surfaces and soil until the model telemetry matched flight data detailing deceleration of the rover with time. The best match was one in which the power law relationship between soil resisting pressure and depth was indicative of hard-packed soil (cohesive strength of ~1 to 3 KPa and angle of internal friction of 30°, values that are typical of slightly cohesive terrerstrial soils) with maximum wheel penetration of

Table 3. Summary of SCLS Thruster Plume Models and Ground Tests[a]

Scour or Test Case	$\frac{\dot{V}}{\dot{m}}\cdot(m^3/kg)$	Average Particle Diameter (m)	Cohesion (Pa)	$\frac{H_{co}}{D_e}$	Thrust Level (%)
Burnside	3.17E-03	-	-	290 - 30	53
Goulburn	4.22E-03	-	-	290 - 30	53
Sleepy Dragon	2.68E-03	-	-	290 - 30	53
Hepburn	5.43E-03	-	-	290 - 30	53
MSL-2	3.18E-03	1.00E-04	1300	35	60
MSL-8	2.08E-03	1.00E-04	1300	35	60
MSL-19	2.54E-02	1.00E-03	0	35	100
PHX-22	4.94E-01	1.50E-05	7500	4.1	100

[a]Last four rows show test results. Soil properties for scours at the Bradbury Landing Site are consistent with soil properties used in the Mars Science Laboratory MSL-2 and MSL-3 ground tests. Second column is the ratio of soil volume erosion rate to plume mass inflow rate, and the fifth column is the ratio of engine cutoff altitude to engine nozzle exit diameter.

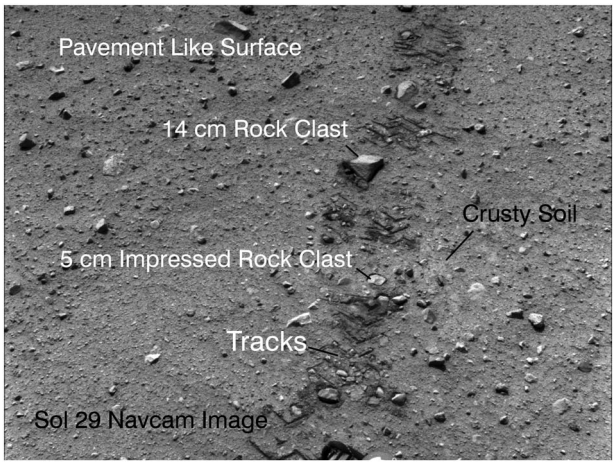

Figure 11. Portion of a Navcam image acquired on sol 29 showing hard-packed soils and traversed rocks. NLA_400071053RAS_F0040000NCAM00408M.

~1 cm. The minimal wheel penetration is consistent with the very low penetration depths calculated from stereo images acquired of the wheel touch down location after Curiosity drove away and imaged the landing zone (Figure 8). Models with cohesionless sandy soil with a 3 to 6 cm in thickness over bedrock produced 2 to 3 cm of wheel penetration, which is not observed for the imprints left by Curiosity's wheels (Figure 8).

The results quoted in the previous paragraph are also consistent with the nature and depth of wheel tracks observed during drives across HP surfaces, i.e., minimal wheel sinkage (<1 cm) because of the hard-packed nature of the soil and embedded rock clasts (Figures 11 and 12). In addition, traverses across relatively large rocks caused the wheels to lift above the soil surface and thus not leave tracks, whereas rocks smaller than ~5 to 8 cm in width were for the most part pressed into the surface because of the smaller area and higher ground pressures (Figure 11). Only a few cases were observed in which rocks were broken by the wheels, and these correspond to exposures of alluvial conglomerate that underlies at least part of the BF surface. Otherwise, the 500–600 N wheel loads (value depends on rover pose and whether the front, middle, or rear wheel is being considered) were insufficient to cause rock fracturing during wheel passages. The lack of fracturing provides a lower bound on the unconfined uniaxial compressive strength for rocks, although the exact stress needed to fracture a rock depends on the rock size and shape and pose of the rover during its passage over a given rock. For example, for the 14 cm wide clast shown in Figure 11, the basal area is about 0.02 m^2 and assuming ~550 N typical wheel load the ground pressure resisting imprinting the rock into the soil would have been ~30 KPa. The soil was hard enough to resist without much sinkage and the rock strength was greater than this normal stress, resulting in lifting of the wheel above the surface and slightly rotating the rock during wheel passage. A brief survey of rocks traversed by Curiosity and comparisons to Mars Yard and field tests using the Scarecrow rover (3/8 mass of Curiosity and used to test drive modes and rover performance on Earth) [e.g., *Heverly et al.*, 2014] is consistent with unconfined compressive strengths typical of consolidated terrestrial sandstones and shales, although the unbroken Mars rocks could be stronger since what is retrieved is a lower bound. On the other hand, the conglomerate bedrock underlying the landing site area must be relatively poorly cemented since wheel traverses across these materials did in some cases lead to rock fracturing.

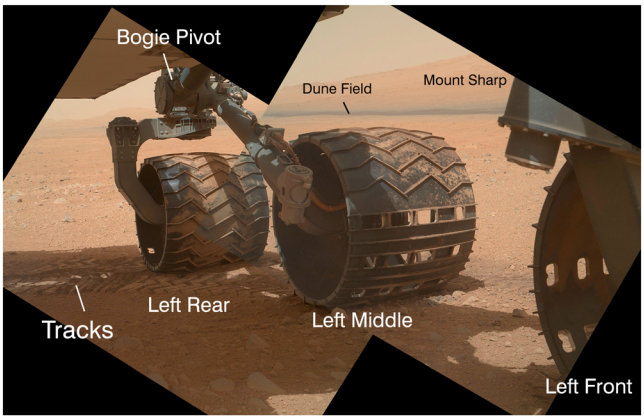

Figure 12. MAHLI image mosaic of left wheels on surface taken on sol 34. Wheel sinkage is minimal, consistent with hard-packed soils typical of HP surfaces. Note the abundant rock clasts and dune field in background.

6. Analysis of ChemCam Laser-Induced Pits

The ChemCam instrument is a a Laser-Induced Breakdown Spectrometer (LIBS) that imparts a focused laser beam at 1.067 μm onto a small spot on the surface [*Maurice et al.*, 2012; *Wiens et al.*, 2012]. The laser, which is located on the mast, produces a beam that volatilizes the rock or soil target at the grain scale, forming an expanding shockwave that excavates an ablation cavity or pit. Emission lines from the cooling plasma expanding behind the

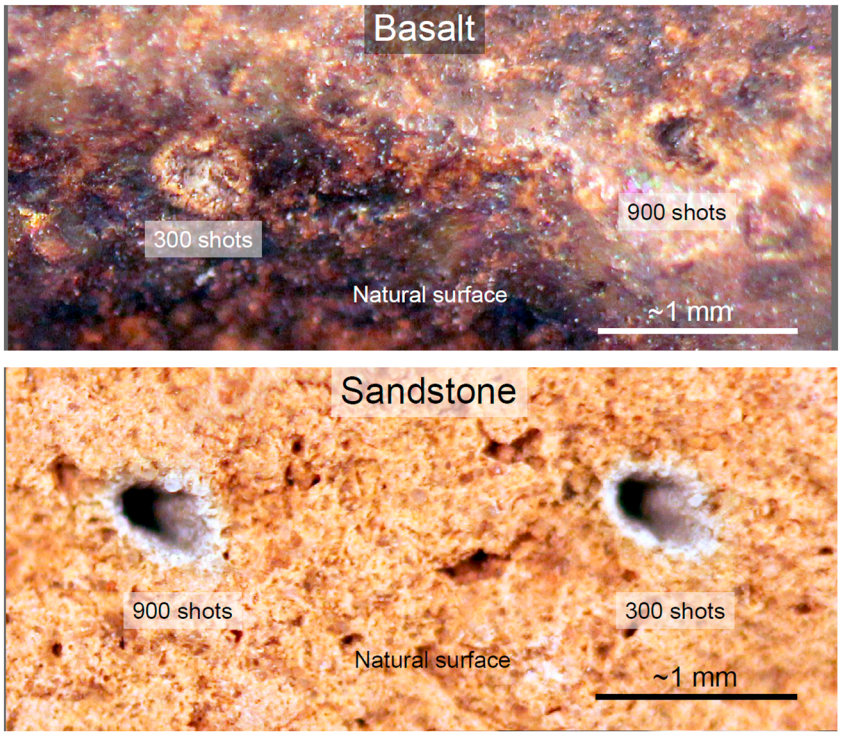

Figure 13. Pits produced by the ChemCam engineering unit in the laboratory in two different rock types. The top image shows ablation pits from 300 and 900 shot analyses on the natural surface of a fine-grained basalt with a rock varnish coating (see N. L. Lanza et al., submitted manuscript, 2014 for more details on this analysis). The bottom image shows ablation pits from 300 and 900 shot analyses on a carbonate-bearing sandstone. Despite the same number of laser shots, the sandstone pits are far deeper than those in the basalt as the result of difference in hardness between the two rock types.

shockwave are sensed with the Chemcam spectrometer and the ablation pits are imaged with the Chemcam Remote Mast Imager (RMI). The laser is usually commanded to direct 30 to 50 shots at the same location to remove dust coatings and probe the composition of the underlying rock or soil target. The size of the pit created depends on the coupling of the beam to the target (related to the focus precision and the target optical and thermal properties), distance (i.e., decreasing irradiance with increasing distance), mechanical properties of the target (strength, texture), and ambient conditions [e.g., *Vadillo et al.*, 1999; *Russo*, 1995; *Sallé et al.*, 2007; *Cousin et al.*, 2012].

Laboratory tests conducted on an aluminum plate show that the ChemCam laser spot size ranges from 360 μm at a range of 1.5 m to 550 μm at a 7 m range [*Maurice et al.*, 2012], and similar pit widths should be expected on Mars for the same ranges, modulated for the factors mentioned in the previous paragraph. Figure 13 shows pits generated by hundreds of shots from a 3 m standoff distance in the laboratory using an engineering model of the ChemCam mast unit. Laser parameters were similar to ChemCam with a laser power of ~13 mJ/pulse and a repetition rate of 3 Hz. Samples were placed in a chamber under 933 Pa CO_2 pressure to simulate collection under Martian conditions. The beam was close to, but not always, perpendicular to the sample surface due to the uneven nature of the natural rock surfaces. Pit widths and depths are larger for the relatively weak carbonate-bearing sandstone as compared to those in the fine-grained, well-indurated basalt, although care must be used in inferring rock type and induration from pit characteristics with only two laboratory tests. It should be noted that ChemCam in flight typically does far fewer shots (30–50) than were done on the laboratory samples (300–900), and thus, the lab-based pits represent maximum diameters relative to what would be expected from flight data.

Numerous ChemCam laser-induced ablation pits have been imaged on Mars using the RMI camera, which has an angular resolution of ~20 μrad/pixel (S. Le Mouélic et al., The ChemCam remote microimager at Gale Crater: Review of first year on Mars, submitted to *Icarus*, 2014), translating into a spatial resolution of 40–120 μm/pixel for the 2 to 6 m distances ranges typical for laser shots. Pit widths

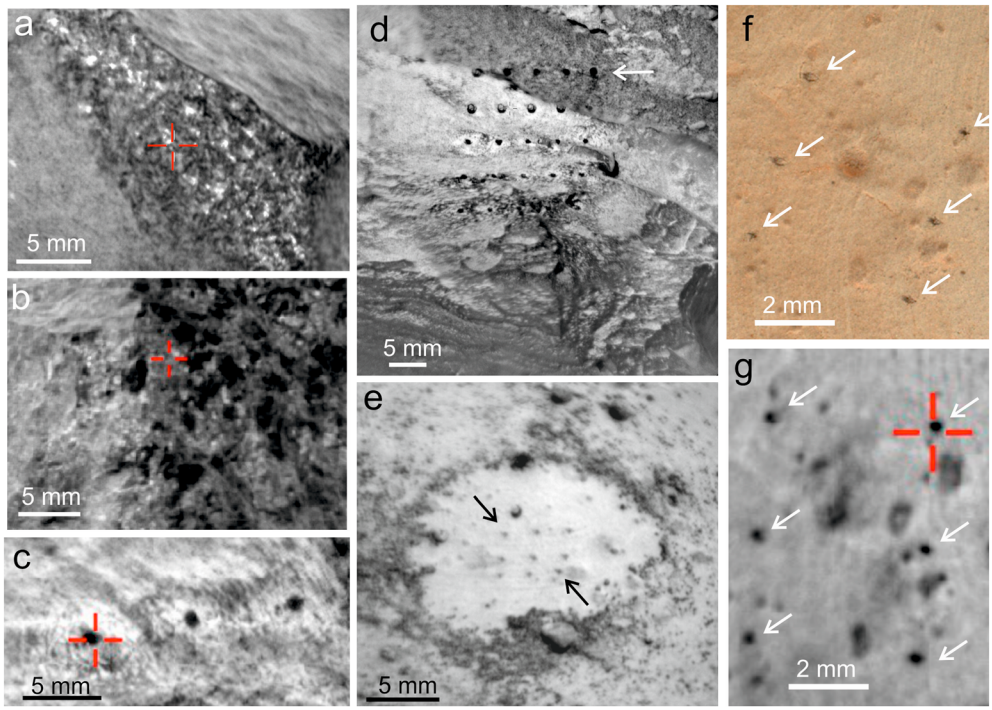

Figure 14. A series of ChemCam laser ablation pits for rocks is shown as follows, with portions of RMI images shown: (a) RMI image CRO_414813474EDR_F0060000CCAM2195M1 of Coronation (sol 13). The laser ablated the surface at the red cross without making a pit. (b) CRO_398826604EDR_F0030004CCAL05015M1 on target Mara (sol 15). A pit was not produced. (c) CRO_406722703EDR_F0050388CCAM1104M1 of the target Acasta (sol 104). (d) CRO_40546821EDR_F0050104CCAM01089M2 of the target Rocknest3_Top (sol 90). The white arrow shows where the fifth row of laser shots encountered soil. (e) RO_41373664EDR_F0060000CCAM01183M1 of Wernecke_Raster1 (sol 183). (f) MAHLI image 173MH0227000000RO_DXXX and (g) CRO_412759482EDR_F0060000CCAM01172M1 of target Wernecke 1 (sol 172). Pits shown in the RMI image are the same as those observed on the MAHLI image. The higher resolving power for MAHLI shows that the pits are not exactly circular, likely because of relatively high laser incidence angles and textural irregularities. Even so the mean diameters based on RMI data are useful estimates of pit diameters.

are reported as the average of horizontal and vertical diameters on RMI images to minimize distortions from tangential shots. LIBS pits are generally conical but are at times horseshoe shaped in plan view, due in part to slight irregularities in the energy density profile of the beam [*Maurice et al.*, 2012; also see *Wiens et al.*, 2012, Figure 31; *Lanza et al.*, 2014]. The irregular pits in rock targets also show the importance of rock texture in determining pit characteristics, including the effects of spallation of rock fragments, in addition to azimuthally homogeneous ejection of plasma, vapor, and particles.

Example, pits in rocks and soils are shown in Figures 14 and 15a, and a plot of pit width as a function of range is shown in Figure 15b. Coronation and Mara rock targets (Figures 14a and 14b), which are located in the HP, do not show obvious pits, even at maximum resolution. These targets are indurated, coarse-grained rocks with basaltic compositions based on color and textural analysis from Mastcam images and ChemCam compositional data [*Yingst et al.*, 2013; *Sautter et al.*, 2013]. In contrast, most rock targets in Rocknest and Yellowknife Bay display pits. For example, the pits on the Acasta target (Figure 14c) are 0.6 ± 0.1 mm. In addition, Figure 14d shows a 5×5 matrix of pits associated with measurements of rock target Rocknest_3. The topmost points hit the surrounding soil. Rock pits on this target vary from 0.6 mm (first series at bottom) to 1.4 mm (fourth row), a diameter wider than what expected from lab analysis at this distance, and as wide as the pits in the surrounding soils. The large pit diameters for the fourth row are likely due to a relatively thick coating of soil. The rock target Wernecke (Figures 14e–14g) in the Sheepbed mudstone unit in Yellowknife Bay was imaged with RMI and Mars Hand Lens Imager (MAHLI) after a 3×3 matrix of laser pits was generated on a bright area

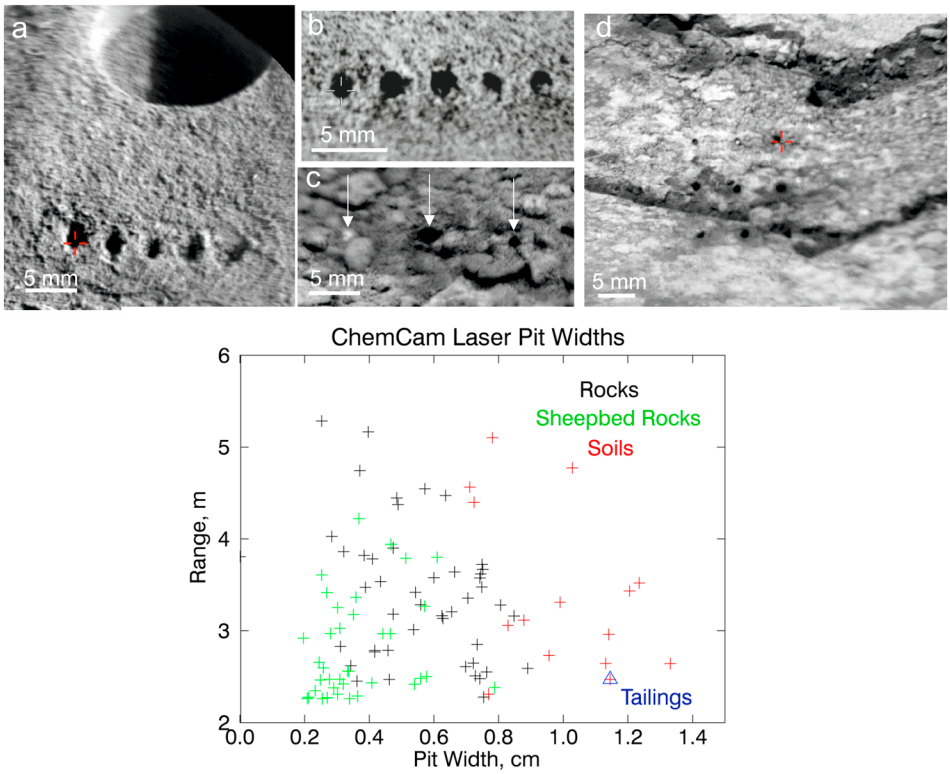

Figure 15. (top) A series of ChemCam laser ablation pits in soils as follows: (a) CRO_414813474EDR_F0060000CCAM2195M1 of the John Klein drill tailings (sol 195). (b) CRO_404936786EDR_F0050104CCAM3083M1 on target Crestaurum soil (sol 84). (c) CRO_401308772EDR_F0041632CCAM03043M1 on target Kam (sol 43). (d) CRO_409476672EDR_F0051858CCAM3135M1 of the target Pachi (sol 135). (bottom) Plot of laser pit width as a function of distance to the target for all surfaces for which pits were observed through sol 180. This provides a good sampling of pits for both the hummocky plains and bedded fractured units. Soils exhibit larger pit diameters for a given range relative to rocks, except for the Sheepbed mudstone targets. Tailing target is the powder that accumulated next to the John_Klein drill site on the Sheepbed mudstone unit.

where the surface was cleaned of dust using the brush on the robotic arm. Pits are relatively small (~0.3 mm in diameter), given the 2.5 m laser range. In fact, Sheepbed targets have the lowest pit widths as a function of range for rock targets. This is inferred to be a consequence of a slight degree of cohesion that is not enough for the shockwave to cause rock spalling, but enough to slightly inhibit excavation of grains. Results are also consistent with the low power needed for drilling into the Sheepbed targets John-Klein and Cumberland [*Grotzinger et al.*, 2014].

A scatterplot of pit diameter as a function of laser range for rocks and soils is presented in Figure 15 and shows that soils typically have larger widths for given ranges relative to rocks, except for the Sheepbed mudstone unit. The drill tailings soil is a very fine grained, cohesionless powder that accumulated around the drill site on this unit (Figure 15a). Pits in this powder have an average diameter of 1.2 mm and a maximum of ~2 mm (Figure 15, bottom). Pits in the cohesionless wind-blown sand target Crestaurum at Rocknest (Figure 15b) vary between 1 and 2 mm in diameter. The similarity to the tailings pit widths implies that cohesion is a controlling parameter in determining pit widths in fine-grained soils. Pebbly soils display significant variations in pit diameters. For example, three pits were generated in the HP Kam soil target. Figure 15c shows from right to left, a 0.9 mm diameter pit for a relatively coarse-grained target, a 1.5 mm diameter pit for a finer-grained target, and a lack of obvious pit where the laser hit a pebble. Finally, the Pachi soil target (Figure 15d), which was Rocknest soil compacted by the rover wheel, has pit diameters ranging from 0.6 to 0.9 mm in diameter. This observation reinforces the importance of cohesion in addition to grain size in determining pit width, since compaction induces cohesion as fine grains are pressed into pores between larger grains.

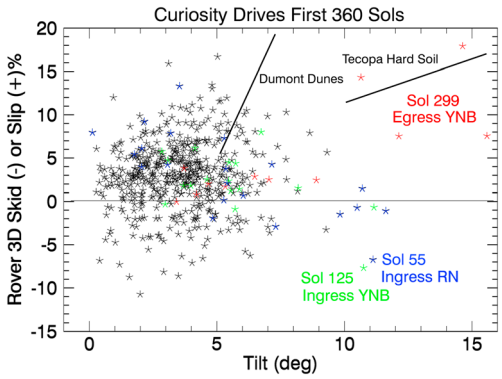

Figure 16. Slip versus tilt for the first 360 sols overplotted with lines representing field data for the Scarecrow rover in the Mojave Desert (described in text). Note that skid (negative slip) occurred during entry into Yellowknife Bay on sol 125 (green coded), whereas slip occurred during the exit on sol 299 (red coded). Skid also occurred during the sol 55 downhill drive to reach Rocknest (RN) (blue coded) at the entrance to Yellowknife Bay.

7. Modeling Curiosity Mobility System as a "Virtual Instrument"

In this section a summary is presented for how telemetry and other data collected during Curiosity's drives were used to retrieve terramechanics properties. The centerpiece of the approach is use of the Artemis numerical mechanical model, which was originally developed to simulate drop tests [*White et al.*, 2012]. It was augmented with wheel azimuth and drive actuators in a manner similar to what was done for the Spirit and Opportunity mechanical models [*Zhou et al.*, 2014]. Grousers are included in the Artemis model since they are part of Curiosity's wheels, and they provide additional thrust as the wheels move along the surface. Artemis allows simulations of Curiosity's drives across digital terrain models derived from HiRISE and/or Navcam stereo images, with inclusion of spatially varying soil properties. The wheel-surface model computes the normal and shear stresses for a set of cells for which the wheels are in contact with the soil surface and then integrates over the total contact area for small time steps to determine the thrust needed to keep the wheels moving at commanded angular velocities, e.g., along specified Ackerman Arcs. Normal and shear stresses between the wheels and soil are modeled using the classical Bekker-Wong-Reece terramechanics expressions that describe relationships among normal stress, wheel sinkage, and shear stress as a function of deformable soil properties [e.g., *Wong*, 2001]:

$$\sigma = \left(k_c/b + k_\varphi\right) z^n \tag{2}$$

$$\tau = \left(c + \sigma \tan\left(\varphi\right)\right)\left(1 - e^{-j/kx}\right) \tag{3}$$

where σ is the normal stress between the wheel and soil, k_c/b is the ratio of soil cohesion modulus to wheel width, k_φ is the internal friction modulus, z is the depth of wheel sinkage, n is a scaling exponent, τ is the shear stress, c is the soil cohesion, φ is the soil angle of internal friction, j is the slippage value between the wheel and soil, and k_x is the shear modulus in the longitudinal or drive direction. The value for j is based on the magnitude of wheel sinkage into soil.

These basic equations have been converted to a wheel cylindrical geometry as summarized in numerous papers and books [e.g., *Wong*, 2001]. Surface properties are retrieved for drives across bedrock and deformable soils in Artemis by registering flight-based rover pitch, wheel sinkage (from Navcam and hazard avoidance camera (Hazcam) stereo imaging data), and the sign and magnitude of rover 3-D slippage (from VO measurements) as a function of position along the model drive paths. The Opportunity and Curiosity versions of the model have been validated using terrestrial experiments on hard-packed soils (effectively bedrock with little to no sinkage) and dune sands [*Stein et al.*, 2013; *Heverly et al.*, 2014; *Zhou et al.*, 2014].

Curiosity 3-D slippage as a function of tilt, derived from Curiosity VO measurements and accelerometer data, respectively, for the first 360 sols, are shown in Figure 16. For reference, field-based test data in the Mojave Desert derived from the "Scarecrow" engineering version of Curiosity (3/8 mass to simulate loads on Mars) are overlain onto this scatterplot, showing the relatively high slip regime for dune sand in the Dumont Dunes and lower regimes for hard-packed soil covering lacustrine bedrock outcrops in the Tecopa area [*Heverly et al.*, 2014]. The retrieved k_x value (shear deformation modulus) for the dune data is 28 mm, whereas a value of 8 mm was retrieved for the hard-packed soil drives [*Stein et al.*, 2013]. Larger values correspond to higher slip values for a given shear stress at the wheel-soil interface. The dunes consist of well-rounded, well-sorted, cohesionless sands, and the relatively high value k_x is consistent with higher slip for a given shear stress as compared to the hard-packed soils covering the lacustrine bedrock units in the Tecopa area.

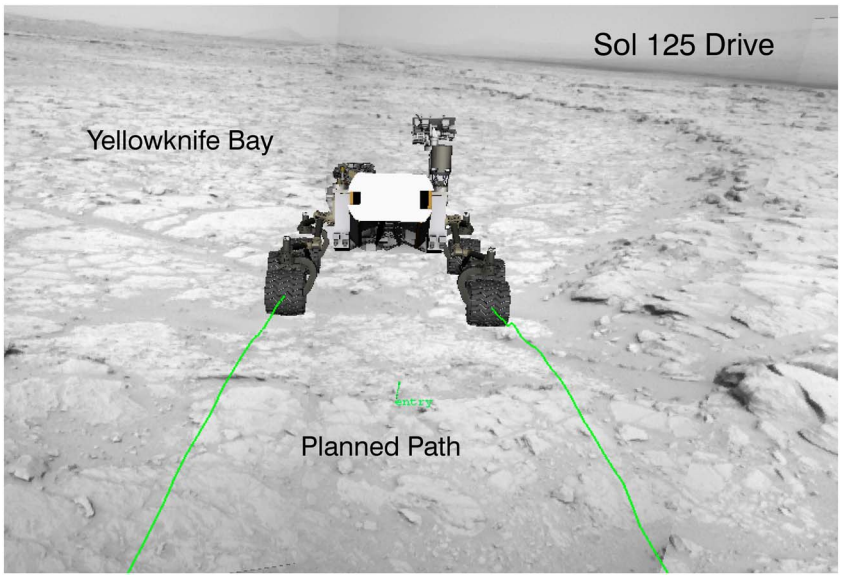

Figure 17. Navcam image perspective view taken on sol 124 showing sol 125 planned drive into Yellowknife Bay, with graphic showing Curiosity to scale relative to the terrain. Navcam frame NLA_408507598RAS_F0051216NCAM00219M.

Curiosity slippage as a function of tilt data show that the rover experienced skid while descending into Yellowknife Bay to access wind-blown sand in the Rocknest area (Figure 16). Skid was also experienced while driving into YKB to access the Sheepbed mudstone unit. On the other hand, the egress out of YKB led to high slippage as the rover worked against the downhill component of its weight. As noted in a previous section of this paper minimal wheel sinkage (~1 cm or less based on analysis of Navcam and Hazcam stereo images of wheel tracks) dominated drives during the first 360 sols. This implies that compaction resistance due to soil compression has been minimal, and that rover tilt has been the primary control on slippage (sign and magnitude), in contrast to drives with Spirit on the Gusev plains and Inner Basin [*Arvidson et al*., 2010] and

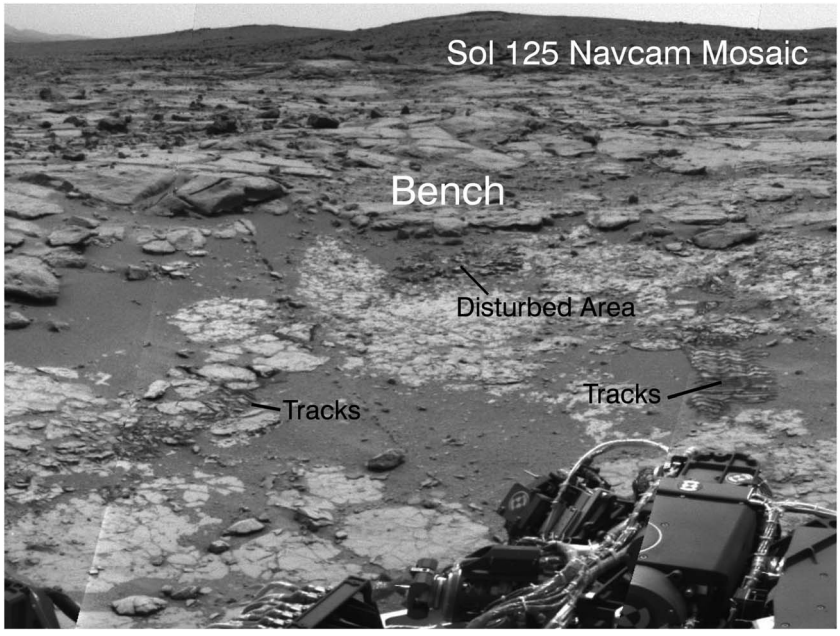

Figure 18. Navcam image acquired on sol 125 looking at sol the 125 drive into Yellowknife Bay. Only tracks that are evident are when the rover crossed soil patches. Navcam frames NLA_408589361XYZLF0051348NCAM03894M1.

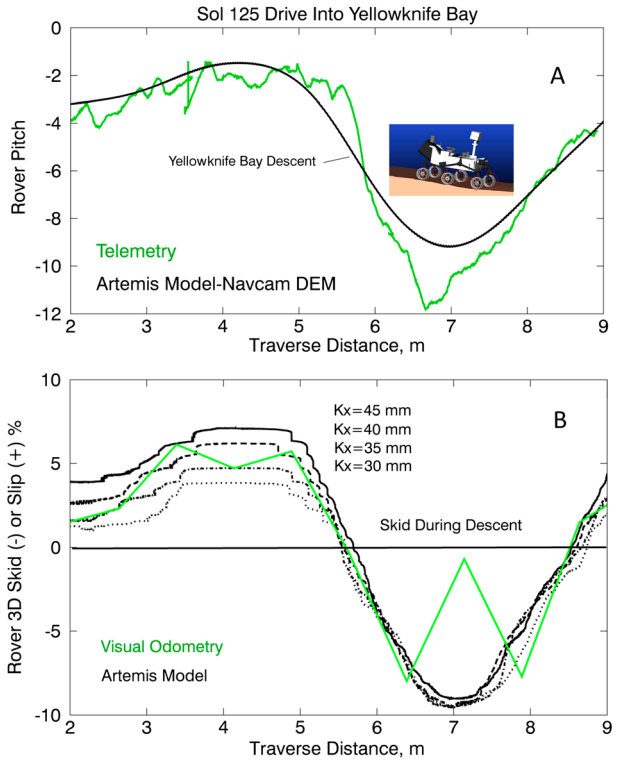

Figure 19. (a) Drive pitch and (b) slip compared to Artemis model results for the portion of the sol 125 drive when Curiosity descended into Yellowknife Bay. Negative pitch corresponds to traveling downhill for the forward drive that occurred on this sol. Lack of soil sinkage indicates that compaction resistance can be ignored, and the downhill component of rover weight was by far the most important element in the force balance with the thrust from the driven wheels. In this case the vehicle actually went further than the commanded wheel angular velocities because the weight of the vehicle was tilted in the drive direction, i.e., skid was observed. VO-based slip and skid data are overlain with Artemis models with different shear modulus values. Top model curve corresponds to highest-shear modulus value and bottom one to lowest value. See text for detailed discussion.

with Opportunity traversing across wind-blown ripples in Meridiani Planum [*Arvidson et al.*, 2011; *Zhou et al.*, 2014]. Two Curiosity drive segments (BF and HP surfaces) are modeled to quantify this inference.

7.1. Yellowknife Bay Bedrock Drive

During the sol 125 drive into YKB Curiosity crossed over several rock layers that lie beneath the HP surfaces and descended onto BF surfaces where the Sheepbed mudstone is exposed (Figures 17 and 18). To model the descent into YKB, a DEM was extracted from the sol 126 Navcam stereo coverage looking back at the bench (Figure 19). The locations of slippage values (from VO) acquired during the drive were determined by cross comparisons with telemetry files that included wheel-based rover positions and accelerometer-based tilts, all organized by onboard clock time. Models were constructed for a drive from the relatively flat area to the south of the bench, north across the bench, and down onto the relatively flat exposures of Sheepbed mudstone.

Artemis was run iteratively until results for a given rover pitch reproduced both the sign and magnitude of slippage during descent into YKB. Examination of Navcam and Hazcam images acquired looking back at the drive path showed minimal wheel sinkage (Figure 18) and no obvious scraping of the bedrock. The pressure-sinkage relationship (equation (1)) was set to keep the sinkage to <1 cm (Table 4). A retrieved k_x value of 40 mm best fits the slippage data, including significant rover skid during the steepest portion of the descent into YKB (Figure 19). The high value of k_x is not surprising given that the drives were on minimal soil and platy bedrock exposures without much texture, i.e., surfaces that would produce significant slip for given applied shear stresses.

Table 4. Artemis Model Values for Normal and Shear Stress Wheel-Soil Contact Parameters Shown in Equations (2) and (3)[a]

Parameter	Sol 125 BF Drive	Sol 344 HP Drive
k_c/b	100/0.5	100/0.5
k_φ	100	100
n	1.4	1.4
c	1.5 KPa	1.5 KPa
φ	30°	30°
k_x	40 mm	20 mm

[a]By far most of the variance in the flight data was modeled by choosing the appropriate value of k_x, given the minimal sinkage and associated compaction resistance.

7.2. Sol 344 Drive on the Hummocky Plains

A segment of the ~70 m drive conducted on sol 344 was chosen to be representative of the terrain topography and surface characteristics of the HP surfaces encountered during the first 360 sols. A representative 10 m segment was modeled in which VO was used to calculate slip magnitude and sign. Cross comparisons were conducted between locations for slippage determination and rover positions to localize rover pitch as a function of slip, using clock times as a way organize the data. Mastcam (Figure 20), Navcam, and Hazcam

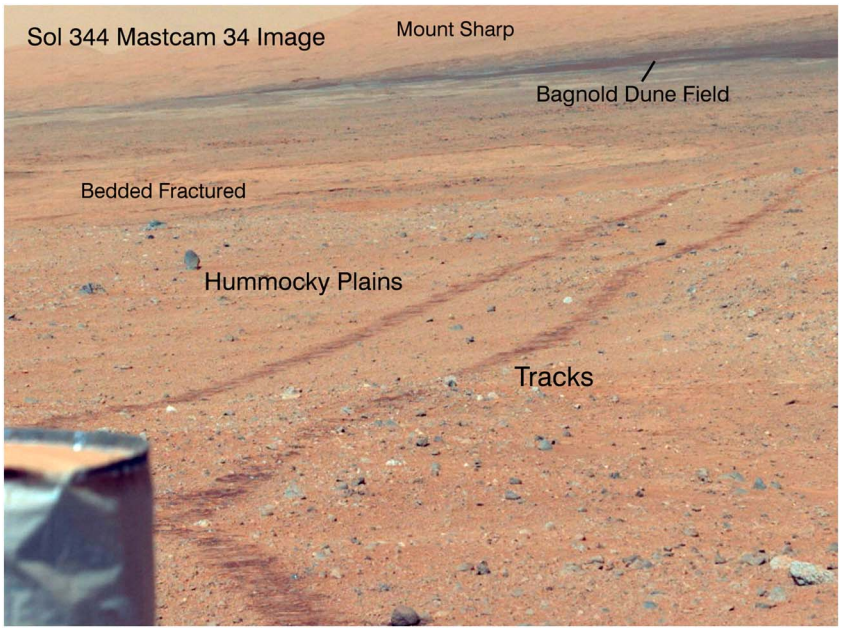

Figure 20. Mastcam color image showing tracks and hummocky plains terrain driven over on sol 344. Dark tracks are evident and interpreted to be due to the wheels pushing dust into the dark underlying basaltic sands. Wheel sinkage into the soil is minimal and estimated from Navcam and Hazcam stereo images. Both embedded and surface rock clasts are evident and strewn across the pavement-like surface. The bedded fractured surface can be seen in the left portion of the image. Mastcam image ML__428042260EDR_S0100000MCAM01396M.

data looking back at the tracks left during the sol 344 drive showed that the ubiquitous bright dust layer covering the rock clast-strewn basaltic soil was disturbed by pressing dust into the underlying soils, leaving dark tracks. Sinkage based on these data and a Mars Descent Imager (MARDI) image data acquired during twilight after the drive (Figure 21) was found to be minimal, with cleat imprints and disturbance of soil clods, but not appreciable wheel sinkage. Small rocks were pressed into the soil, whereas large rocks were either not disturbed or rotated, but not imprinted into the underyling soil during wheel passages. Given the relative lack of wheel sinkage and associated compaction resistance, the main resistance to motion was vehicle downhill weight component, with slippage controlled largely by the value of k_x.

Artemis models were run using a digital elevation model derived from sol 343 Navcam data and wheel sinkage values kept to <1 cm. The k_x values were adjusted iteratively to match the slippage values (sign and magnitude) as a function of rover pitch (Figure 22). The modeled drive segment was chosen to have variable pitch as the rover climbed a gentle rise. This allowed variation in pitch to provide variation in slippage, thus allowing retrieval of reasonable k_x values. The modeled drive segment began ~8 m into the drive, and the Navcam-based elevation model only generally reproduced pitch as a function of time. The drive through the depression is represented. The best retrieved k_x is 20 mm, which is less than the value for the descent into YKB and still in the range for typical terrestrial soils [*Wong*, 2001]. Exploratory Artemis models for other drives on HP surfaces produced similar results and show that the value for slip for a given shear stress is less on the rock strewn hard-packed soil that dominates HP surfaces as opposed to the bedrock-dominated BF surfaces. This result is not surprising given the complex textures on the HP surfaces, including embedded and surface rock clasts and granule to dust-sized soils. Driven wheels undergo less slip for given loads and shear stresses because of this complex textural pattern, particularly when the grousers traverse over rocks clasts.

8. Implications for Landscape Evolution

This paper has focused on the physical properties of the surfaces and near surfaces for the HP and BF surfaces that Curiosity has traversed during the first 360 sols of the mission. Analyses of orbital data were used to provide a regional-scale context, and analyses of Curiosity descent, landing, driving, and laser-induced

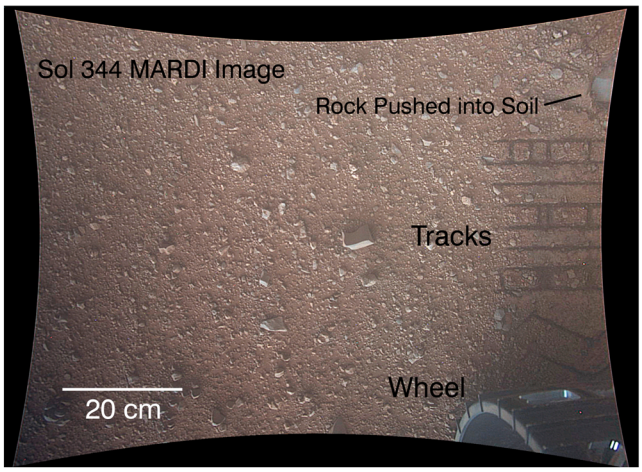

Figure 21. MARDI view of sol 344 tracks taken at the end of drive. Note the abundance of rock clasts that form a pavement-like surface. Wheel track shows minimal sinkage and largely consists of grouser imprints. A small rock in the upper right of the image has been pushed into the soil. MARDI image MD__428055785EDR_F0100000MRDI00069M.

ablation pit data were used to enable a more detailed understanding of terrain properties. Results also have implications for the evolution of the HP and BF landscapes, as described below.

HP surfaces are dominated by dusty, hard-packed, poorly sorted basalt sands with embedded and surface rock clasts overlying bedrock deposited as a coalescing alluvial fan system (Figure 23). When combined with the abundance and variable degradation states of impact craters seen from orbit and from Curiosity (Figure 3; H. E. Newsom et al., Gale crater and impact processes—Observations during Curiosity's first 360 sols on Mars, submitted to *Journal of Geophysical Research: Planets*, 2014)

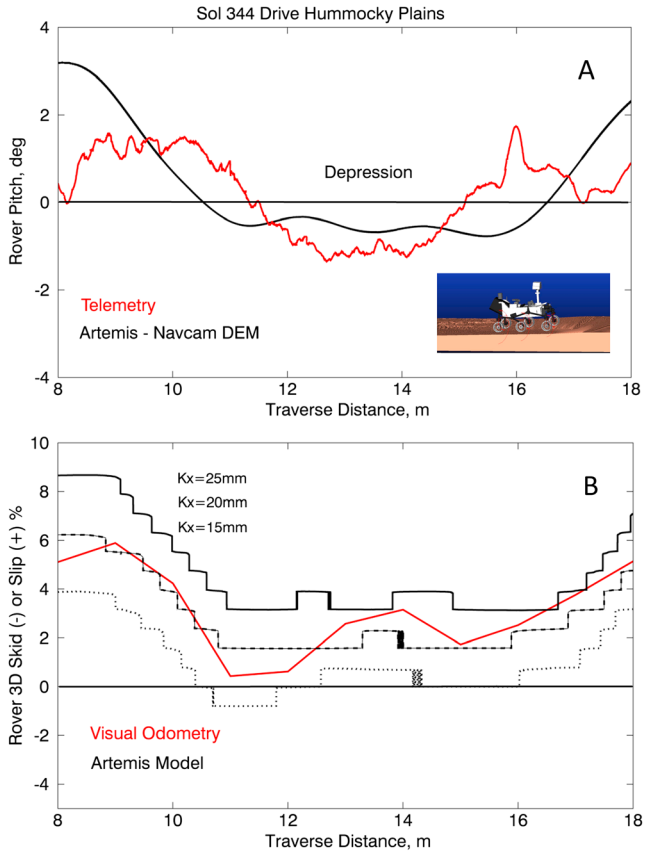

Figure 22. (a) Drive pitch and (b) slip for a portion of the sol 344 drive compared to Artemis model results. This forward drive segment begins with a positive pitch and then becomes negative as the rover traverses across a depression, climbing out toward the end with a positive pitch. Measured slip remained positive throughout and was modeled with varying shear modulus values. See text for detailed discussion.

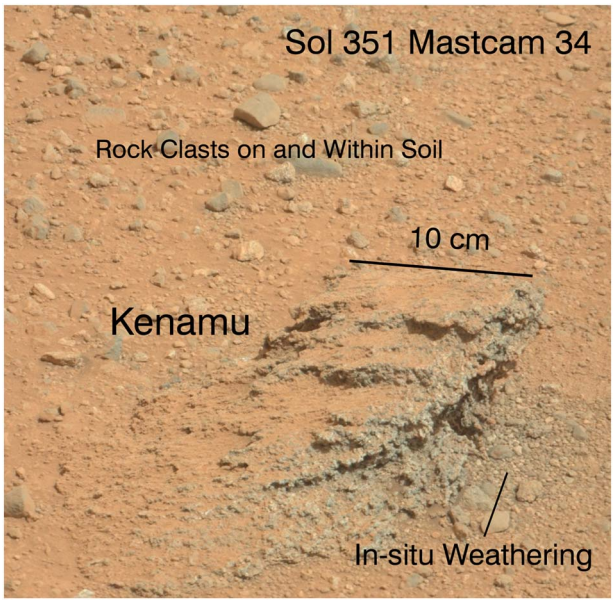

Figure 23. Mastcam color image acquired on sol 351 of conglomerate rock Kenamu weathering in place on the hummocky plains. Note the rounded pebbles accumulating beneath the rock. Embedded and surface rocks clasts are evident around Kenamu. Mastcam image MR__428645916EDR_S0110000MCAM01429M.

a conceptual model can be outlined for the evolution of HP surfaces. Accumulation of the coalescing alluvial fan materials occurred as impact cratering and aeolian processes were also shaping the surface. Fan accumulation slowed and then stopped, whereas impact cratering continued to modify the surface, as did wind erosion, transport, and deposition. Bedrock with varying degrees of consolidation was exposed by wind stripping and weathered in situ to add rock clasts, pebbles, and sands to the evolving soil layer (Figures 23, 24a, and 25). Impacts added ejecta on both local and regional scales, and craters formed and were subsequently degraded by additional impacts, mass wasting, and wind-related processes. HP surfaces became covered with a dense rock clast pavement. Wind-deposited sands in protected areas such as Rocknest and other rock clusters and generally

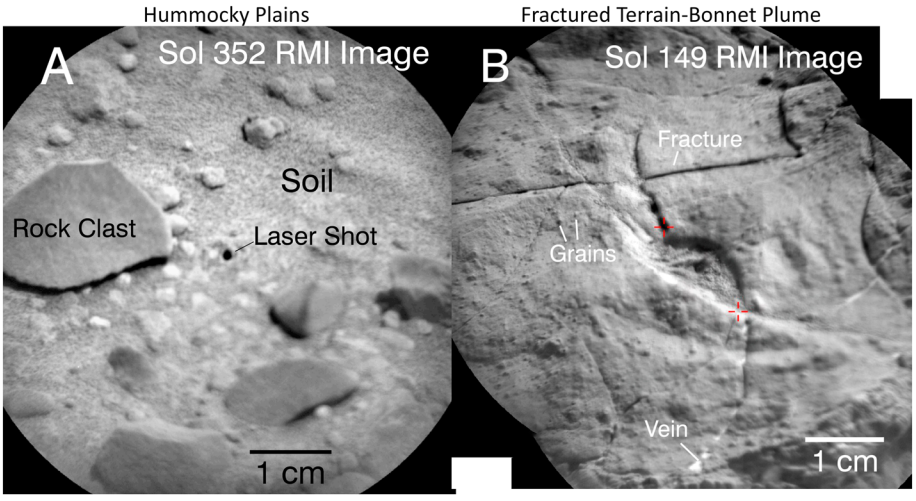

Figure 24. Sol 352 RMI image representative of the hummocky plains surface, together with a sol 149 RMI mosaic image of Bonnet-Plume, a flat rock target in Yellowknife Bay. Although covering only relatively small area, these two images are representative of the dense coverage of rock clasts of a variety of sizes and shapes for hummocky plains surfaces and the extensive bedrock exposures for the Mudstone unit. RMI images CR0_428737249EDR_F0110302CCAM15022L1, CR0_410727034EDR_F0051902CCAM01149M1, and CR0_410727995EDR_F0051902CCAM01149M1, respectively.

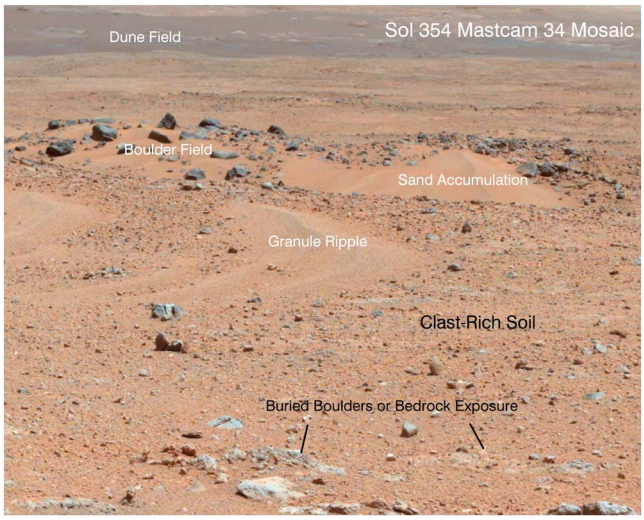

Figure 25. Sol 354 Mastcam color mosaic showing hummocky plains terrain elements, including the pavement-like surface, patchy exposed outcrops, wind-blown ripples, and sands trapped in boulder fields. For scale the granule ripple wavelength is ~1.4 m.

added a thin layer of poorly sorted basalt sand and a dust cover across the whole area (Figure 22). Local ripples accumulated. Minor wetting events probably produced crusty soils cemented by minor amounts of sulfates, which seem to be ubiquitous across Mars. The combination of processes discussed above produced the complex array of features and physical properties evident in Curiosity-based images of HP surfaces (Figure 22).

The BF landscape must have evolved in a manner similar to the evolution of the HP landscape, with impact cratering and wind-related activity occurring during and after alluvial, fluvial, and lacustrine processes and associated deposition slowed and stopped. Fan deposition may have occurred within YKB after deposition of the HP deposits, although this inference is not unique [*Grotzinger et al*., 2014]. Alternatively, the BF units represent older strata that underlie the bedrock found on and near the HP surfaces traversed by Curiosity. The relative lack of soil cover on the BF surfaces (e.g., Figure 24b, a flat rock) and the thin soil cover on HP surfaces also imply efficient wind-induced stripping of loose material over the long term.

Acknowledgments
We thank NASA for support for our work on MSL and CRISM, and we thank the science and engineering teams associated with the Mars Science Laboratory, HiRISE, CRISM, and THEMIS for planning and acquisition of the data used in this paper. Data are available from the NASA Planetary Data System Geosciences Node (http://pds-geosciences.wustl.edu/).

References

Arvidson, R. E., et al. (2004), Localization and physical properties experiments conducted by Spirit at Gusev Crater, *Science*, *305*(5685), 821–824, doi:10.1126/science.1099922.

Arvidson, R. E., et al. (2006), Overview of the Spirit Mars Exploration Rover Mission to Gusev Crater: Landing site to Backstay Rock in the Columbia Hills, *J. Geophys. Res.*, *111*, E02S01, doi:10.1029/2005JE002499.

Arvidson, R. E., et al. (2010), Spirit Mars Rover Mission: Overview and selected results from the northern Home Plate Winter Haven to the side of Scamander Crater, *J. Geophys. Res.*, *115*, E00F03, doi:10.1029/2010JE003633.

Arvidson, R. E., et al. (2011), Opportunity Mars Rover Mission: Overview and selected result from Purgatory Ripple to traverses to Endeavour Crater, *J. Geophys. Res.*, *116*, E00F15, doi:10.1029/2010JE003746.

Arvidson, R. E., et al. (2014), Ancient aqueous environments at Endeavour Crater, Mars, *Science*, *343*, doi:10.1126/science.1248097.

Bish, D., et al. (2013), X-ray diffraction results from Mars Science Laboratory: Mineralogy of Rocknest at Gale Crater, *Science*, *341*, doi:10.1126/science.1238932.

Blake, D., et al. (2013), Curiosity at Gale Crater, Mars: Characterization and analysis of Rocknet sand shadow, *Science*, *341*, doi:10.1126/science.1239505.

Christensen, P. R., et al. (2004), The Thermal Emission Imaging System (THEMIS) for the Mars 2001 Odyssey Mission, *Space Sci. Rev.*, *110*, 85–130, doi:10.1023/B:SPAC.0000021008.16305.94.

Clark, R. N. (1999), Chapter 1: Spectroscopy of rocks and minerals, and principles of spectroscopy, in *Manual of Remote Sensing, Volume 3, Remote Sensing for the Earth Sciences*, edited by A. N. Rencz, pp. 3–58, John Wiley, New York.

Cousin, A., V. Sautter, C. Fabre, S. Maurice, and R. C. Wiens (2012), Textural and modal analyses of picritic basalts with ChemCam laser-induced breakdown spectroscopy, *J. Geophys. Res.*, *117*, E10002, doi:10.1029/2012JE004132.

Fergason, R. L., P. R. Christensen, M. P. Golombek, and T. J. Parker (2012), Surface properties of the Mars Science Laboratory landing sites: Characterization from orbit and predictions, *Space Sci. Rev.*, *170*, 739–773, doi:10.1007/s11214-012-9891-3.

Ferguson, D., and A. Stentz (2005), The Field D* algorithm for improved path planning and replanning in uniform and non-uniform cost environments, *Tech. Rep. CMU-TR-RI-05-19*.

Fox, V. K., R. E. Arvidson, and M. J. Wolff (2013), Quantifying surface scattering parameters for bright and dark Martian surfaces, Abstract P23F-1861 presented at 2013 Fall Meeting, AGU.

Grotzinger, J. P., et al. (2012), Mars Science Laboratory Mission and science investigation, *Space Sci. Rev.*, *170*, 5–56, doi:10.1007/s11214-012-9892-2.
Grotzinger, J. P., et al. (2014), A habitable fluvio-lacustrine environment at Yellowknife Bay, Gale Crater, Mars, *Science*, *343*, doi:10.1126/science.1242777.
Hamilton, V. E., et al. (2014), Observations and preliminary science results from the first 100 sols of MSL REMS ground temperature sensor measurements at Gale Crater, *J. Geophys. Res. Planets*, *119*, 745–770, doi:10.1002/2013JE004520.
Heverly, M., J. Matthews, J. Lin, D. Fuller, M. Maimone, J. Biesiadecki, and J. Leichty (2014), Traverse performance characterization for the Mars Science Laboratory Rover, *J. Field Robotics*, *30*, 835–846, doi:10.1002/rob.21481.
Huertas, A., Y. Cheng, and R. Madison (2006), Passive imaging-based multi-cue hazard detection for spacecraft landing, paper presented at the 2006 IEEE Aerospace Conference, Big Sky, Mont., March.
Johnson, J. J., et al. (2014), ChemCam passive reflectance spectroscopy of surface materials at the Curiosity landing site, *Icarus*, doi:10.1016/;icarus.2014.02.028, in press.
Jouglet, D., et al. (2007), Hydration state of the Martian surface as seen by Mars Express OMEGA I: Analysis of the 3 μm hydration feature, *J. Geophys. Res.*, *112*, E08S06, doi:10.1029/2006JE002846.
Lanza, N. L., et al. (2014), Understanding the signature of rock coatings in laser-induced breakdown spectroscopy data, *Icarus*, doi:10.1016/j.icarus.2014.05.038, in press.
Leshin, L., et al. (2013), Volatile isotope, and organic analysis of Martian fines with the Mars Curiosity rover, *Science*, *341*, doi:10.1126/science.1238937.
Lichtenberg, K. A., et al. (2007), Coordinated analyses of orbital and Spirit Rover data to characterize surface materials on the cratered plains of Gusev Crater, Mars, *J. Geophys. Res.*, *112*, E12S90, doi:10.1029/2006JE002850.
Maimone, M., Y. Cheng, and L. Matthies (2007), Two years of visual odometry on the Mars Exploration Rovers, *J. Field Robotics*, *24*(3), 169–186, doi:10.1002/rob.20184.
Maurice, S., et al. (2012), The ChemCam instrument suite on the Mars Science Laboratory (MSL) Rover: Science objectives and mast unit description, *Space Sci. Rev.*, *170*, 95–166, doi 10.1007/s11214-012-9912-2 .
McEwen, A., et al. (2007), Mars reconnaissance orbiter's High Resolution Imaging Science Experiment (HiRISE), *J. Geophys. Res.*, *112*, *E05S02*, doi:10.1029/2005JE002605.
Mehta, M., et al. (2011), Explosive erosion during the Phoenix landing exposes subsurface water on Mars, *Icarus*, *211*, 172–194, doi:10.1016/j.icarus.2010.10.003.
Mehta, M., A. Sengupta, N. O. Renno, J. W. Van Norman, P. G. Huseman, D. S. Gulick, and M. Pokora (2013), Thruster plume surface interactions: Applications for spacecraft landings on planetary bodies, *AIAA J.*, *51*, 2800–2818, doi:10.2514/1.J052408.
Meslin, P.-Y., et al. (2013), Soil diversity and hydration as observed by ChemCam at Gale Crater, Mars, *Science*, *341*, doi:10.1126/science.1238670.
Milliken, R. E., J. F. Mustard, F. Poulet, D. Jouglet, J.-P. Bibring, B. Gondet, and Y. Langevin (2007), Hydration state of the Martian surface as seen by Mars Express OMEGA II: H2O content of the surface, *J. Geophys. Res.*, *112*, E08S07, doi:10.1029/2006JE002853.
Morris, R. V., D. Golden, D. Ming, T. Shelfer, L. Jorgensen, J. Bell, T. Graff, and A. Mertzman (2001), Phyllosilicate-poor palagonitic dust from Mauna Kea Volcano (Hawaii): A mineralogical analogue for magnetic Martian dust?, *J. Geophys. Res.*, *106*(E3), 5057–5083, doi:10.1029/2000JE001328.
Murchie, S. L., et al. (2007), Compact Reconnaissance Imaging Spectrometer for Mars (CRISM) on Mars Reconnaissance Orbiter (MRO), *J. Geophys. Res.*, *112*, E05S03, doi:10.1029/2006JE002682.
Putzig, N. E., M. Mellon, K. Kretke, and R. E. Arvidson (2005), Global thermal inertia and surface properties of Mars from the MGS mapping mission, *Icarus*, *173*, 325–341, doi:10.1016/j.icarus.2004.08.017.
Russo, R. E. (1995), Laser-ablation, *Appl. Spectrosc.*, *49*(9), A14–A28.
Sallé, B., P. Mauchien, and S. Maurice (2007), Laser-Induced breakdown spectroscopy in open-path configuration for the analysis of distant objects, *Spectrochim. Acta, Part B*, *62*(8), 739–768.
Sautter, V. C., et al. (2013), Igneous mineralogy at Bradbury rise: The first ChemCam campaign, *J. Geophys. Res. Planets*, *119*, 30–46, doi:10.1002/2013JE004472.
Schieber, J., M. Malin, T. Olson, F. Calef, K. Comeaux, and MSL Science Team (2013), The final 2 1/2 minutes of terror—What we learned about the MSL landing from the images taken by the MARDI descent imager, *44th Lunar and Planetary Science Conference*, abstract #1260.
Sebastián, E., C. Armiens, J. Gómez-Elvira, M. P. Zorzano, J. Martinez-Frias, B. Esteban, and M. Ramos (2010), The rover environmental monitoring station ground temperature sensor: A pyrometer for measuring ground temperature on Mars, *Sensors*, *10*(10), 9211–9231, doi:10.3390/s101009211.
Seelos, K., F. Seelos, S. Murchie, R. Arvidson, and A. Fraeman (2013), Mosaicked hyperspectral CRISM data: Mineralogic variability of the MSL landing site and possible traverse in Gale Crater, *44th Lunar and Planetary Science Conference*, abstract #2814.
Stamnes, K., S. Tsay, W. Wiscombe, and K. Jayaweera (1988), Numerically stable algorithm for discrete-ordinate-method radiative transfer in multiple scattering and emitting layered media, *Appl. Opt.*, *27*, 2502–2509.
Stein, N., R. Arvidson, M. Heverly, R. Lindemann, B. Trease, K. Iagnemma, and C. Senatore (2013), Validation of Artemis mobility simulations for the Spirit, Opportunity, and Curiosity Mars rovers, Abstract #P51G-1826 presented at 2013 Fall Meeting, AGU.
Steltzner, A. D., et al. (2010), Mars Science Laboratory entry, descent, and landing system overview, 2010, in *International Planetary Probe Workshop*, Barcelona, Spain, 12 June.
Stolper, E., et al. (2013), The petrochemistry of Jake_M: A Martian mugearite, *Science*, *341*, doi:10.1126/science.1239463.
Sullivan, R., R. Anderson, J. Biesiadecki, T. Bond, and H. Stewart (2011), Cohesions, friction angles, and other physical properties of Martian regolith from Mars Exploration Rover wheel trenches and wheel scuffs, *J. Geophys. Res.*, *116*, E02006, doi:10.1029/2010JE003625.
Vadillo, J. M., J. M. Fernandez Romero, C. Rodriguez, and J. J. Laserna (1999), Effect of plasma shielding on laser ablation rate of pure metals at reduced pressure, *Surf. Interface Anal.*, *27*(11), 1009–1015.
Vaniman, D., et al. (2014), Mineralogy of a mudstone at Yellowknife Bay Gale Crater, Mars, *Science*, *343*, doi:10.1126/science.1243480.
Vasavada, A. R., et al. (2014), Overview of the Mars Science Laboratory mission: Bradbury Landing to Yellowknife Bay and beyond, *J. Geophys. Res. Planets*, *119*, doi:10.1002/2014JE004622, in press.
White, C., et al. (2012), System verification of MSL Skycrane using an integrated ADAMS simulation, Aerospace Conference, *2012 IEEE March 2012*.
Wiens, R., et al. (2012), The ChemCam instrument suite on the Mars Science Laboratory (MSL) Rover: Body unit and combined system tests, *Space Sci. Rev.*, *170*, 167–227, doi:10.1007/s11214-012.
Williams, R., et al. (2013), Martian fluvial conglomerates at Gale Crater, *Science*, *340*, 1068–1072, doi:10.1126/science.1237317.
Wong, J. (2001), *Theory of Ground Vehicles*, 3rd ed., John Wiley, New York, 9902-4.
Yingst, R. A., et al. (2013), Characteristics of pebble and cobble-sized clasts along the Curiosity rover traverse from Bradbury Landing to Rocknest, *J. Geophys. Res. Planets*, *118*, 2361–2380, doi:10.1002/2013JE004435.
Zhou, F., R. E. Arvidson, K. Bennett, B. Trease, R. Lindemann, P. Bellutta, K. Iagnemma, and C. Senatore (2014), Simulations of Mars Rover traverses, *J. Field Robotics*, *31*(1), 141–160, doi:10.1002/rob.21483.